

---

# **FABRICATION OF MICRO-OPTICS FOR DIODE LASERS AND AMPLIFIERS USING INK-JET TECHNOLOGY**

**W. Royall Cox et al.**

**MicroFab Technologies, Inc.  
1104 Summit Avenue, Suite 110  
Plano, Texas 75074**

**November 1997**

**Final Report**

**APPROVED FOR PUBLIC RELEASE; DISTRIBUTION IS UNLIMITED.**

19971230 081



**AIR FORCE RESEARCH LABORATORY  
Directed Energy Directorate  
3550 Aberdeen Ave SE  
AIR FORCE MATERIEL COMMAND  
KIRTLAND AIR FORCE BASE, NM 87117-5776**

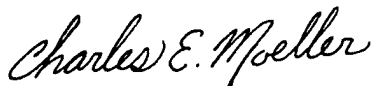
Using Government drawings, specifications, or other data included in this document for any purpose other than Government procurement does not in any way obligate the U.S. Government. The fact that the Government formulated or supplied the drawings, specifications, or other data, does not license the holder or any other person or corporation; or convey any rights or permission to manufacture, use, or sell any patented invention that may relate to them.

This report has been reviewed by the Public Affairs Office and is releasable to the National Technical Information Service (NTIS). At NTIS, it will be available to the general public, including foreign nationals.

If you change your address, wish to be removed from this mailing list, or your organization no longer employs the addressee, please notify AFRL/DE, 3550 Aberdeen Ave SE, Kirtland AFB, NM 87117-5776.

Do not return copies of this report unless contractual obligations or notice on a specific document requires its return.

This report has been approved for publication.

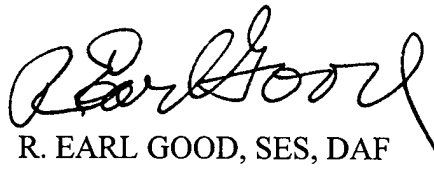


CHARLES E. MOELLER  
Project Officer

FOR THE COMMANDER



GREGORY J. VANSUCH, Maj, USAF  
Chief, Semiconductor Laser Branch



R. EARL GOOD, SES, DAF  
Director, Directed Energy Directorate

REPORT DOCUMENTATION PAGE			Form Approved OMB No. 074-0188	
Public reporting burden for this collection of information is estimated to average 1 hour per response, including the time for reviewing instructions, searching existing data sources, gathering and maintaining the data needed, and completing and reviewing this collection of information. Send comments regarding this burden estimate or any other aspect of this collection of information, including suggestions for reducing this burden to Washington Headquarters Services, Directorate for Information Operations and Reports, 1215 Jefferson Davis Highway, Suite 1204, Arlington, VA 22202-4302, and to the Office of Management and Budget, Paperwork Reduction Project (0704-0188), Washington, DC 20503				
1. AGENCY USE ONLY (Leave blank)	2. REPORT DATE 11/31/97	3. REPORT TYPE AND DATES COVERED Final Technical: 04/19/95 - 10/31/97		
4. TITLE AND SUBTITLE Fabrication of Micro-Optics for Diode Lasers and Amplifiers Using Ink-Jet Technology		5. FUNDING NUMBERS C: F29601-95-C-0059 PE: 65502F PR: 3005 TA: CO PR: HQ		
6. AUTHOR(S) W. Royall Cox, Ting Chen, Rick Hoenigman				
7. PERFORMING ORGANIZATION NAME(S) AND ADDRESS(ES) MicroFab Technologies, Inc. 1104 Summit Ave. Suite 110 Plano, TX 75074		8. PERFORMING ORGANIZATION REPORT NUMBER  PM02		
9. SPONSORING / MONITORING AGENCY NAME(S) AND ADDRESS(ES) Air Force Research Laboratory/DELS 3550 Aberdeen Ave SE Kirtland AFB, NM 87117-5776		10. SPONSORING / MONITORING AGENCY REPORT NUMBER  PL-TR-97-1159		
11. SUPPLEMENTARY NOTES The views, opinions and/or findings contained in this report are those of the authors and should not be construed as an official U.S. Department of the Air Force position or decision, unless so designated by other documentation.				
12a. DISTRIBUTION / AVAILABILITY STATEMENT Approved for public release; distribution unlimited			12b. DISTRIBUTION CODE	
13. ABSTRACT (Maximum 200 Words) A new technology has been developed for fabrication of refractive microlenses using an ink-jet printing method. It offers the advantages of low-cost (no photo lithography, minimal optical material usage) and flexibility (data driven process). Using print heads capable of dispensing picoliter droplets of optical thermal plastic and UV-curing resin formulations at temperatures up to 230° C, both hemispherical and anamorphic plano/convex microlenses have been printed with substrate-plane dimensions ranging from 80 µm to several mm and speeds from f/0.7 to f/5. The specific applications addressed include: arrays of hemi-elliptical microlenses for edge-emitting diode laser array astigmatism correction and coupling into an optical fiber; arrays of hemispherical lenslets for imaging, multiplexing and reflection; and microlenses printed directly onto the tips of optical fibers for increasing numerical aperture for light collection, or onto VCSEL die for focusing into fibers. Optical performance and thermal durability data indicate that these UV-cured printed microlenses would also be suitable for high-power optical interconnects.				
14. SUBJECT TERMS MICRO-OPTICS, INK-JET PRINTING, MICROLENSSES			15. NUMBER OF PAGES 72	
			16. PRICE CODE	
17. SECURITY CLASSIFICATION OF REPORT UNCLASSIFIED	18. SECURITY CLASSIFICATION OF THIS PAGE UNCLASSIFIED	19. SECURITY CLASSIFICATION OF ABSTRACT UNCLASSIFIED	20. LIMITATION OF ABSTRACT UNLIMITED	



## TABLE OF CONTENTS

<u>Section</u>	<u>Page #</u>
1.0 SUMMARY	1
2.0 INTRODUCTION	4
2.1 MICRO-OPTICS FABRICATION AS ENABLING TECHNOLOGY	4
2.2 BACKGROUND ON INKJET / MICROJET PRINTING	5
3.0 MICRO-OPTICS PRINTING METHODS	8
3.1 PRINTING STATION	8
3.2 OPTICAL MATERIALS	9
3.3 PRINTING METHODOLOGY	12
4.0 PRINTED MICROLENSES	15
4.1 CIRCULAR FOOTPRINT MICROLENSES	15
4.1.1 Spherical Microlenses	15
4.1.2 Hyperbolic Microlenses	18
4.1.3 Microlenses Printed onto Optical Fibers	20
4.1.4 Microlens Arrays for Reflectors	21
4.2 ANAMORPHIC MICROLENSES	22
4.2.1 Elliptical Microlenses	22
4.2.2 Cylindrical, Square and Rectangular Microlenses	28
5.0 DIODE LASER COLLIMATION	30
5.1 ADVANTAGES OF PRINTED MICROLENSES	30
5.2 MICROLENS PLACEMENT ALONG BEAM AXIS	31
5.3 ASTIGMATISM CORRECTION	32
6.0 PRINTED MICROLENS CHARACTERIZATION	37
6.1 PLACEMENT, DIMENSIONS AND FOCAL LENGTH	37
6.2 SURFACE CONTOUR UNIFORMITY	41
6.3 POWER POINT SPREAD DISTRIBUTION	43
6.4 MODULATION TRANSFER FUNCTION	46
7.0 PRINTED MICROLENS DESIGN & MODELING	49
7.1 HEMISPHERICAL MICROLENSES	49
7.2 HEMI-ELLIPTICAL MICROLENSES	51
8.0 CONCLUSIONS	55
9.0 REFERENCES	57

## FIGURES

<u>Figure #</u>	<u>Page #</u>
1. Schematic of "Continuous" ink-jet printer.	5
2. Schematic of "Drop-on-Demand ink-jet printer.	6
3. Generation of 50 $\mu\text{m}$ droplets at 2 kHz by DOD micro-jet device.	7
4. Schematic of Micro-optics Printing Station.	8
5. Illustration of moving Shuttle stage to (1) print, (2) UV-cure & (3) view in situ.	8
6. Issues to be considered when optimizing optical material properties for both micro-jet printing and printed microlens performance.	10
7. Comparison for adhesion to untreated (G) and low-wetting glass (TG) and for hardness of 2 thermoplastic (MM-1.7 & RW-122) and a UV-curing resin (MRX-101).	11
8. Focal length of three sizes of microlenses printed with MRX-115, after bakes at temperatures up to 200°C, where variation is within measure error.	12
9. Variation of circular-footprint printed microlens aspect ratio by varying process parameters.	12
10. Array (left) and far-field diffraction pattern (right) of 100 $\mu\text{m}$ diameter hemispherical microlenses printed on 125 $\mu\text{m}$ centers with UV-curing optical material onto low-wetting glass.	15
11. Increase in lenslet diameter with number of 40 $\mu\text{m}$ droplets of UV-curing material deposited onto untreated (Std) and low-wet-treated (LW) glass.	16
12. Increase in focal length with number of 40 $\mu\text{m}$ droplets of UV-curing material deposited onto untreated (Std) and low-wet-treated (LW) glass.	16
13. Variation of microlens focal length with diameter for UV-cure material on untreated (Std) & low-wetting glass and for a high-temperature thermoplastic on untreated glass.	17
14. Four microlenses printed with equal volumes of optical thermoplastic at	17

215°C onto substrates at four different temperatures.

15.	High-fill-factor array of 950 $\mu\text{m}$ hemispherical microlenses, each printed with UV-curing material and flash-cured immediately after its deposition.	18
16.	Profiles of (A) quasi-hyperbolic and (B) spherical microlenses printed with 25 each 40 $\mu\text{m}$ droplets of UV-cure material using 5 each 0.2 sec UV-flashes during and 1 after printing.	19
17.	Microlenses at 150X magnification, printed with (left-to-right) 5, 7 & 9 each 50 $\mu\text{m}$ droplets of MRX-110B UV-curing resin, with automated spot cures after each droplet deposition.	19
18.	Increasing printed microlens aspect ratio by repeating cycles of UV spot-curing after deposition of each 50 $\mu\text{m}$ droplet, from 5 to 9 times (left-to right).	19
19.	140 $\mu\text{m}$ diameter optical fibers with printed microlenses of decreasing radii of curvature as the number of deposited droplets is increased (left-to-right).	20
20.	Angular distribution of normalized power emitted from flat (A) and lensed (B) fiber tips.	20
21.	30 X 30 array of 154 $\mu\text{m}$ diameter MRX-115 microlenses printed onto C6-treated cover glass on 197 $\mu\text{m}$ centers, where back focal lengths have been adjusted (by number of 50 $\mu\text{m}$ droplets deposited at each site) to be at backside of substrate.	21
22.	Portion of above microlens array shown focusing an aperture image at backside of substrate with illumination from top of microlenses.	22
23.	Four each hemi-elliptical microlenses, 284 $\mu\text{m}$ X 146 $\mu\text{m}$ X 20 $\mu\text{m}$ high, viewed in substrate plane (left), "fast" (f/1.5) focal plane (middle) and "slow" (f/3.2) focal plane (right).	23
24.	Two arrays of 4 each hemi-elliptical microlenses printed with 6 each 60 $\mu\text{m}$ droplets of optical thermoplastic on (A) 50 $\mu\text{m}$ & (B) 67 $\mu\text{m}$ centers, shown in (L->R) substrate, "fast" [FL: (A)=432 $\mu\text{m}$ , (B)=362 $\mu\text{m}$ ] and "slow" [FL: (A)=900 $\mu\text{m}$ , (B)=1,543 $\mu\text{m}$ ] focal planes.	23
25.	Variation of hemi-elliptical microlens axes and axis ratio (width/length) in substrate plane with spacings of 6 deposited 60 $\mu\text{m}$ droplets.	24
26.	Variation of hemi-elliptical microlens focal lengths and focal length ratio with spacing of 6 deposited 60 $\mu\text{m}$ droplets.	24

27.	Two hemi-elliptical microlenses printed with 10 each 60 $\mu\text{m}$ droplets of optical thermo-plastic on 50 $\mu\text{m}$ centers, shown in (A) “fast” and (B) focal planes and in profile along (C) minor and (D) major axis.	25
28.	Hemi-elliptical microlenses printed with 6 each 60 $\mu\text{m}$ droplets of UV-curing optical material in the vertical direction on center-to-center spacings varying in increments of 10 $\mu\text{m}$ from (a) 25 $\mu\text{m}$ to (h) 95 $\mu\text{m}$ .	26
29.	Variation with droplet spacing of focal lengths and dimensions of hemi-elliptical lenslets of Fig. 28.	26
30.	Hemi-elliptical microlenses at 60X magnification, printed by depositing indicated number of 50 $\mu\text{m}$ droplets of MRX-115 at 6 sites on 125 $\mu\text{m}$ centers.	27
31.	Variation of dimensions in substrate plane and fast and slow focal lengths (left scale), along with focal length ratio (right scale), of printed hemi-elliptical lenslets, with number of 50 $\mu\text{m}$ droplets deposited at each of six sites on 125 $\mu\text{m}$ centers.	27
32.	165 $\mu\text{m}$ wide, 37 $\mu\text{m}$ high, printed cylindrical microlenses shown in (left) focal plane and (right) in profile, where focal length is 215 $\mu\text{m}$ (f/1.3).	28
33.	Array of 300 $\mu\text{m}$ square, 50 $\mu\text{m}$ high optical thermoplastic microlenses printed on 400 $\mu\text{m}$ centers shown in (left) focal plane (FL=227 $\mu\text{m}$ ) and (right) in profile.	28
34.	Array of 300 $\mu\text{m}$ X 870 $\mu\text{m}$ rectangular lenslets on 500 $\mu\text{m}$ centers shown in (left) substrate and (right) focal (FL=375 $\mu\text{m}$ ) planes.	29
35.	Illustration of potential use of custom-printed array of hemi-elliptical microlenses in collimating the diverging outputs of an edge emitter diode laser arrays to maximize efficiency of geometric multiplexing into a fiber.	30
36.	Illustration of axial positioning optimization for edge-emitting diode laser collimation.	31
37.	Transmitted diode laser beam divergence in two planes as a function of plano/convex microlens axial position within back focal plane of lenslet.	32
38.	Amplified spot widths versus beam profiler moving distance along optical axis, from which astigmatism for this for this diode laser is calculated using optical system amplification factor.	33
39.	Series of UV-cured microlenses, each printed by depositing droplets at three	33



	sites and increasing the distance between sites (L-to-R) by 20 $\mu\text{m}$ per lenslet, resulting in a gradual increase in ellipticity (Length/Width).	
40.	Variation of focal lengths and substrate plane dimensions with site spacings for UV-cured microlenses printed with 3 each depositions of 333 each droplets per lenslet.	34
41.	Axial movements required for each of 9 hemi-elliptical microlenses of Fig.1 to move between “fast” and “slow” focal planes of diode laser, for two depicted lenslet orientations relative to laser “fast” (most rapidly diverging) direction.	34
42.	Images of diode laser beam waist transmitted by differently printed 1 mm hemispherical microlenses, showing significantly less distortion for the vertically printed one on the right.	35
43.	Data demonstrating the 2 $\mu\text{m}$ spatial stability over extended periods of time of 50 $\mu\text{m}$ droplets, microjetted at 5,000 Hz and stroboscopically “frozen” in space and time.	38
44.	10 each repeated 3" Shuttle-stage translations & printings at 150°C of a 60 $\mu\text{m}$ droplet of optical thermoplastic.	38
45.	Distribution of diameters of vertically printed hemispherical microlens of MRX-115 material within a 100 lenslet array, showing standard deviation of 1.2% (5.9 $\mu\text{m}$ ) from average diameter of 494 $\mu\text{m}$ .	39
46.	Distribution of focal lengths of the 100 vertically printed, 0.5 $\mu\text{m}$ diameter microlenses for which diameter data are given in Figure 45, showing standard deviation from the average value of 1.5%.	39
47.	Experimental setup for obtaining interference ring patterns from individual microlens for qualitative comparisons of uniformity of shape and surface smoothness.	41
48.	Interferometric pattern of 120 $\mu\text{m}$ diameter hemi- <u>spherical</u> microlens printed with optical thermoplastic at 215°C.	41
49.	Interferometric pattern from a slightly damaged and mis-shaped hemi-spherical microlens.	42
50.	Interferometric pattern of 304 $\mu\text{m}$ X 196 $\mu\text{m}$ hemi- <u>elliptical</u> microlens printed with optical thermoplastic.	42

51.	Interferometric pattern of 212 $\mu\text{m}$ wide <u>square</u> shaped microlens printed by deposition of 3X3 pattern of 50 $\mu\text{m}$ droplets of optical thermoplastic.	42
52.	Relative intensity versus scan distance for 127 $\mu\text{m}$ diameter, 1.08 diffraction-limited lenslet printed with <u>one</u> 50 $\mu\text{m}$ droplets of UV-curing material.	43
53.	2D power distribution of focal spot for 1-drop lenslet of Fig. 52.	44
54.	3D focal plane power distribution of N=1 lenslet of Fig.52.	44
55.	Focal peak for 223 $\mu\text{m}$ diameter, 1.04 diffraction-limited lenslet printed with <u>ten</u> 50 $\mu\text{m}$ droplets of UV-curing material.	45
56.	Power scans across “fast” (left) & “slow” (right) focal lines of a printed hemi-elliptical microlens lens from the array shown above in “fast” & “slow” focus planes, at 300 $\mu\text{m}$ & 1,864 $\mu\text{m}$ from substrate plane.	45
57.	Experimental configuration for measuring Modulation Transfer Function of a microlens.	46
58.	Point Spread Function (PSF) for a microlens printed with one 50 $\mu\text{m}$ droplet of MRX-115 optical resin, shown as irradiance versus distances in microns in the focal plane.	47
59.	Line Spread Function (LSF) calculated from Fig. 2 for the printed 1-drop microlens, shown as irradiance versus distance in microns, where FWHM is 1 $\mu\text{m}$ .	47
60.	Typical Modulation Transfer Function of a 1-drop microlens printed with MRX-115 UV-curing resin, compared to theoretical result for same $f/\#$ (1.25).	48
61.	Model of printed hemispherical microlens as cap cut from a sphere of radius R, where a, h & $\theta$ are microlens substrate-plane-radius, height & substrate contact angle, respectively.	49
62.	Comparison of measured and calculated (from diameter and contact angle) heights and calculated (from diameter and focal length) numerical apertures for a range of printed hemispherical microlenses.	51
63.	Hemi-elliptical lens cut from top of an ellipsoid with radii a,b,c, having major & minor substrate-plane axis radii of $a_1$ & $b_1$ and height h.	52
64.	Comparison of measured and calculated focal lengths for hemi-elliptical thermoplastic microlenses as a function of deposited droplet spacing.	54

## PREFACE

This is the Final Technical Report for the work performed under an SBIR (Small Business Innovative Research) Phillips Laboratory contract # F29601-95-C-0059. The overall objective of this work has been to develop a commercially viable technology for the fabrication of micro-optical interconnects by the ink-jet/micro-jet printing method for use in the manufacture of optoelectronic packages and systems. The particular focus of the effort has been to develop data-driven processes for *in-situ* printing of microlenses onto optical substrates and components for low-cost and efficient coupling of the outputs of diode lasers and amplifiers to optical fibers and detectors. The motivation for this work has been the potential advantages of this technology over conventional methods of micro-optics manufacture in many significant applications, which include: (a) the lowering of manufacturing costs (no photo-lithography); (b) the capability for direct "writing" of micro-optical elements onto optoelectronic components as a final, "value-added" step; and (c) the flexibility to customize the positions and characteristics of printed microlenses within each array to maximize coupling performance for a given source (e.g., by compensating for imperfections in emitter alignment in stacked diode laser bars).

This report summarizes the methods developed under this contract for the microjet printing of a wide variety of microlens configurations with both commercial and specially developed optical materials. Photographs and physical properties of these various types of printed microlenses are presented, along with corresponding optical performance data. Conclusions are drawn regarding the capabilities and potential usefulness in optoelectronics manufacturing of this Micro-optics Printing Technology, along with its potential for wide spread commercialization. Details about the experimental methods developed and progress made toward commercialization are provided in other reports to Phillips Laboratory.

The authors would like to thank, firstly, our chemical consultant, Michael E. Grove, for developing and supplying the custom optical material formulations, without which we could not have developed a *commercially* viable technology for microlens printing. Secondly, we express

our appreciation to Dr. Ron Maruzak and Dr. Hans-Jochen Trost, formerly and currently of MicroFab Technologies, respectively, for developing the software packages and computer interfaces utilized on the R&D Micro-optics Printing Station. In addition, we thank our optical consultant, Prof. Duncan E. MacFarlane and his students, Brian Teipen and Jim Tatum at the University of Texas at Dallas, for developing systems and methods for detailed optical characterization of our printed microlenses. Finally, we would like to express special appreciation to Dr. Charles Moeller of the Phillips Laboratory, our Technical Project Monitor, for the encouragement and helpful suggestions he has provided throughout the course of this contract.

## 1.0 SUMMARY

A new technology has been developed for the fabrication of refractive microlenses for use in collimating and focusing output beams from diode lasers and amplifiers. It utilizes ink-jet printing methods for dispensing optical material and forming microlenses directly onto optical substrates, components, and optoelectronic packages. The general advantages of this method over conventional techniques of micro-optics fabrication for many applications include low-cost (single-step, no photo lithography masks, no material waste), flexibility (data-driven process), automated (PC controlled) and non-contact (print *in-situ* on flat or curved substrates). Specific advantages for diode laser and amplifier optical interfacing to optical fibers and detectors are the capabilities for printing microlenses or lenslet arrays which are customized in both shape and location to maximize the coupling efficiency for each source component or array during final assembly.

This work has leveraged MicroFab's core technologies for manufacturing drop-on-demand print heads capable of dispensing picoliter quantities of materials at temperatures up to 240°C and for formulating ink-jet-printable optical materials, in order to develop a highly viable, microlens printing technology. The components of this technology include: (a) an automated Micro-optics Printing Station with *in-situ* printing, UV-curing and a target substrate vision system; (b) optical thermoplastic and UV-curing materials with good optical and mechanical/thermal-durability properties; and (c) processes for printing a wide variety of microlens configurations.

The printed plano/convex microlens configurations shown and discussed here may be divided into two categories, namely, those having a circular "footprint" on the substrate and those which do not, i.e., those classified as anamorphic. Among the circular-footprint microlenses for which printing processes were developed are those having either spherical or hyperbolic cross-section perpendicular to the substrate. These lenslets are printed by depositing one or more droplets, typically 50  $\mu\text{m}$  in diameter, onto a target site and either solidifying/curing the droplets *in-situ* after depositing all of the droplets, or between droplet bursts, respectively. By varying process

parameters such as type of optical material deposited and size & number of droplets, along with temperature and wetting characteristics of the substrate, the printing of microlenses with diameters as small as 80  $\mu\text{m}$  and speeds ( $f/\# = \text{focal-length/diameter}$ ) over the range 0.7 - 5 was accomplished. The configurations of anamorphic microlenses printable with this technology include those with ellipsoidal, cylindrical cross-sections perpendicular to the substrate, in addition to those with square and rectangular substrate footprints. Microlenses printed with the UV-curing optical materials have transmission above 95% in the near-IR, refraction index variable from 1.5 to 1.7, and ability to withstand temperatures to 200°C without degradation of optical properties.

One application investigated for printed microlenses is arrays of hemi-elliptical lenslets for collimation of edge-emitting diode laser arrays, in order to optimize the efficiency of geometric multiplexing into an optical fiber or detector. Here adjustment of the ratio of "slow" and "fast" focal lengths provided by the elliptical configuration enables correction of laser astigmatism by bringing differently diverging outputs to focal waists in same plane, while the placement of individual lenslets on the substrate may be adjusted to compensate for laser-bar registration errors. Experiments were performed to determine the degree of ellipticity required to correct the astigmatism of a typical edge-emitting diode laser. Other applications explored included microlenses printed onto the tips of optical fibers to increase numerical aperture for capturing light from diode laser emitters and onto substrates as arrays for use in de-multiplexing and/or focusing of collimated sources or for retro-reflection applications.

The dimensional and focusing properties of printed microlenses were fully characterized for all configurations and sizes. Repeatability of substrate-plane dimensions and focal lengths for nominally identical microlenses within an array were within  $\pm 1\%$  and 2%, respectively. An interferometric system was developed for testing symmetry and uniformity of lenslet surfaces. Spherical aberrations in printed hemispherical microlenses were studied using measurements of focal-plane power point-spread-distribution peaks and modulation transfer function, and the data indicated that these lenslets exhibit nearly diffraction limited performance.

Design models were developed for predicting dimensions of both spherical and elliptical microlenses required to meet pre-set optical performance specifications, assuming that such lenslets may be approximated by caps cut from spheres and ellipsoids, respectively. Agreement between experimentally measured and model-derived theoretical values of printed lenslet parameters was found to be good.

It may be concluded from this work that microlens printing is a highly viable technology which could be leveraged to advantage in many optoelectronic manufacturing applications. This conclusion is based both upon the capabilities demonstrated and upon the high levels of interest expressed by potential commercial users.

## 2.0 INTRODUCTION

### 2.1 MICRO-OPTICS FABRICATION AS ENABLING TECHNOLOGY

The continued evolution of information transmission and processing systems will increasingly rely on advanced micro-optics fabrication technologies to connect optically the various pieces of optoelectronic systems, in order to resolve bottlenecks resulting from high circuit density, multiple pin-outs, high data and processing rates, etc. Capabilities have been evolving for fabricating practical optical interconnects, in the form of micro-optical waveguides<sup>1</sup>, fibers and free-space interconnects<sup>2</sup>, between instrument backplanes, printed circuit boards (PCB's) and electro-optic components within boards. The critical issues for optical interconnects are utilization of materials and processes compatible with electronic circuit board processing and low cost manufacturing through passive optical alignment procedures.<sup>3</sup>

This evolution in micro-optical interconnect technologies is being fueled by the development of new interconnect fabrication processes utilizing organic polymeric materials, which offer significant advantages over the traditional inorganic materials in both electro-optical properties and ease of fabrication.<sup>4</sup> Techniques emerging for utilizing these materials for fabrication of free-space optical interconnects include the micro machining and melting of photo lithographically formed cylinders of photoresist<sup>5</sup> and the use of plastic molding methods<sup>6</sup>.

Microjet printing of polymeric microlenses, as a non-contact, data-driven process, potentially could provide both significant reductions in costs and increases in the flexibility of manufacturing of optoelectronic packages and interconnect components, in addition to enabling new optical-interconnect device configurations which are not possible or practical with other fabrication methods.



## 2.2 BACKGROUND ON INK-JET / MICRO-JET PRINTING

The phenomena of uniform drop formation from a stream of liquid issuing from an orifice were noted as early as 1833 by Savart<sup>7</sup> and described mathematically by Lord Rayleigh<sup>8,9</sup> during 1878-1892. Rayleigh extended his analysis to viscous jets,<sup>10</sup> but the complexity of the relationships makes it of little utility. Weber<sup>11</sup> used a similar approach as Rayleigh, but produced a much more useful result by making several simplifying assumptions.

In the type of system that is based on their observations, fluid under pressure issues from an orifice, typically 50 to 80  $\mu\text{m}$  in diameter, and breaks up into uniform drops by the amplification of capillary waves induced onto the jet, usually by an electromechanical device that causes pressure oscillations to propagate through the fluid. The drops break off from the jet in the presence of an electrostatic field, referred to as the charging field, and thus acquire an electrostatic charge. The charged drops are directed to their desired location, either the catcher or one of several locations on the substrate, by another electrostatic field, the deflection field. This type of system is generally referred to as "continuous" because drops are continuously produced and their trajectories are varied by the

amount of charge applied.

Theoretical and experimental analysis of continuous type devices, particularly the process of disturbance growth on the jet that leads to drop formation, has been fairly extensive.<sup>12,13</sup> **Figure 1** shows a schematic of this type of ink-jet printing system. Such a system is

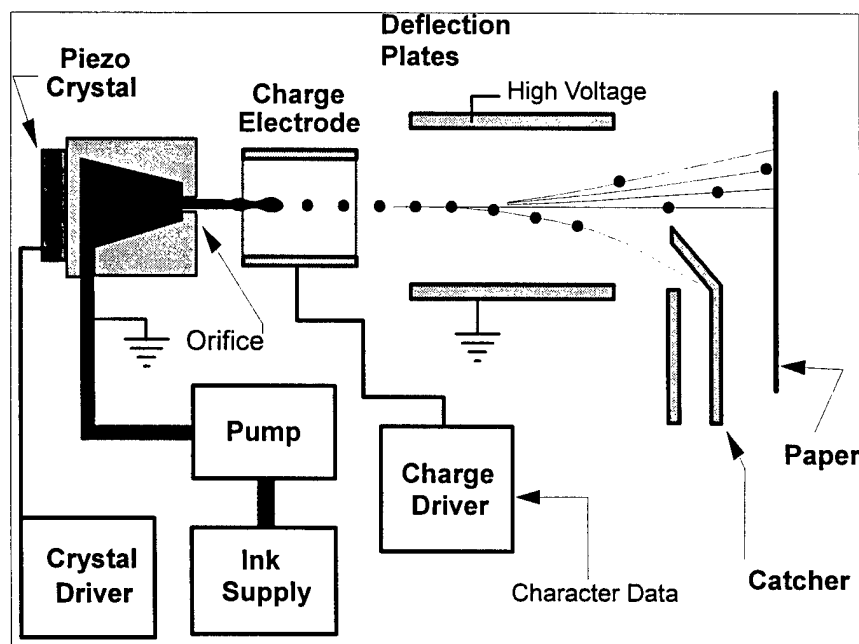


**Figure 1.** Schematic of "Continuous" ink-jet printer.

utilized where high speed is of greater importance than precision, such as in the marking and labeling industry.

In the 1950's, the production of drops at *ambient* pressure by electro induced pressure waves was observed by Hansell.<sup>14</sup> In this type of system, a

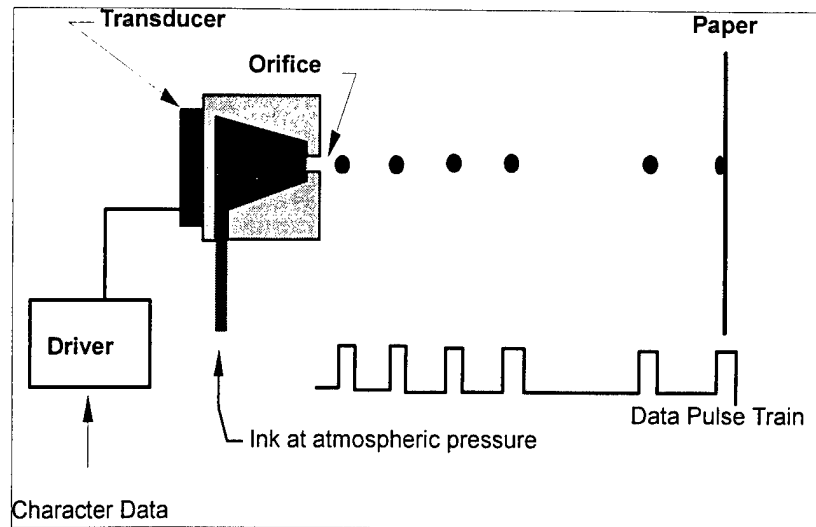


**Figure 2.** Schematic of "Drop-on-Demand" ink-jet printer.

volumetric change in the fluid is induced by the application of a voltage pulse to a piezoelectric material which is directly or indirectly coupled to the fluid. This volumetric change causes pressure/velocity transients to occur in the fluid and these are directed to produce a drop that issues from an orifice.<sup>15,16</sup> Since the voltage is applied only when a drop is desired, these types of systems are referred to as "drop-on-demand" (DOD). In many commercially available ink-jet printing systems, a thin film resistor is substituted for the piezoelectric drive transducer. When a high current is passed through this resistor, the ink in contact with it is vaporized, forming a vapor bubble over the resistor. This vapor bubble serves the same functional purpose as the piezoelectric transducer. **Figure 2** shows a schematic of a drop-on-demand type ink-jet system, which is both simpler in design than the continuous system and eliminates the need to recycle the fluid being printed. Demand mode ink-jet printing systems produce droplets that are approximately equal to the orifice diameter of the droplet generator.<sup>17</sup> The drop-on demand mode of printing is utilized for all office printers and for the micro-optics printing application described in this report.

One of the characteristics of ink-jet printing technology that makes it attractive as a precision fluid micro dispensing technology is the *repeatability* of the process. **Figure 3** shows a MicroFab drop-on-demand type ink-jet device generating 50  $\mu\text{m}$  diameter drops of ethylene glycol from a

device with a 50  $\mu\text{m}$  orifice at 2,000 per second. The image of droplets shown here was made by illuminating the droplets with an LED that was pulsed at the droplet generation frequency. The exposure time of the camera was  $\sim 1$  second, so that the images represent 2000 events superimposed on each other.

The repeatability of the process results in an extremely clear image of the droplets, making it appear to be a high speed photograph and illustrating the precision of the droplet formation process.

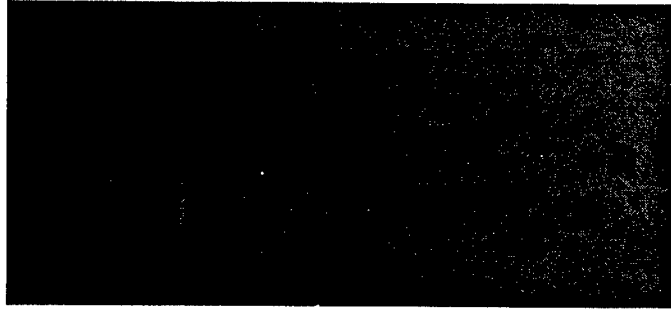


**Figure 3.** *Generation of 50  $\mu\text{m}$  droplets at 2 kHz by DOD micro-jet device.*

### 3.0 MICRO-OPTICS PRINTING METHODS

#### 3.1 PRINTING STATION

The R&D Micro-optics Printing Station is illustrated schematically in **Figure 4**. All of its functions (except switching from vacuum to back-pressure) are computer controlled and automated. The critical element of the system is the print head, which consists of a vertically oriented heated fluid reservoir and proprietary dispensing device, capable of being heated to temperatures as high as 240°C. Other key subsystems include: temperature-controlled vacuum chuck on XY-substrate-translation stages for positioning target substrate; shuttle stage for positioning print head, UV light pipe and vertically oriented targeting microscope alternatively along the print axis; horizontally oriented jet-viewing microscope alternatively along the print axis; horizontally oriented

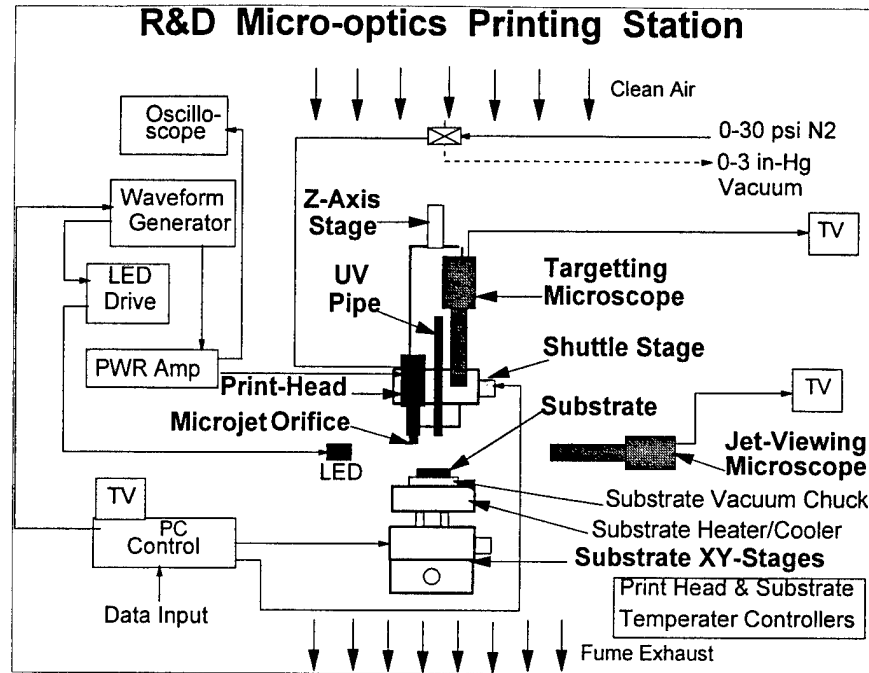


**Figure 4.** Schematic of Micro-optics Printing Station.

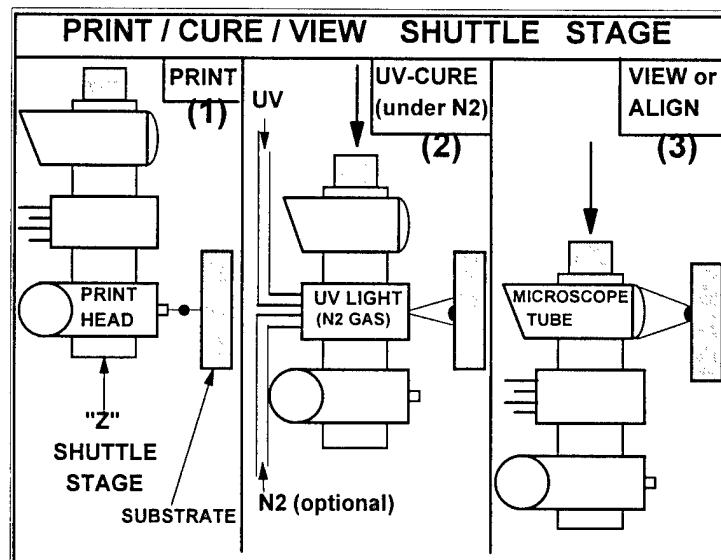


**Figure 5.** Illustration of moving Shuttle stage to (1) print, (2) UV-cure & (3) view in situ.

microscope with LED sight source strobed at device pulsing frequency for observing microjetted droplets during device tuning; printing device driving electronics; and computer for controlling and coordinating all stage motions, driving waveform and sequencing of dispensing events.

The Shuttle stage which alternatively positions the print head, UV-curing head or alignment microscope along the horizontal printing axis, as indicated in **Figure 5**. It enables initiation of UV-cure or direct observation of printed element at any time during the printing process, in addition to alignment to printed features. Again, the sequencing of these events is automated and software driven. The back-pressure at the print head fluid reservoir may be held slightly negative for printing or pressurized by pulses of nitrogen gas to "purge" the dispensing device. Finally, a balanced system of class 100 clean air input and fume exhaust has been installed during this contract, and all three motion control stages have been upgraded with optical encoders.

### 3.2 OPTICAL MATERIALS

The micro-optics printing process imposes a unique set of requirements on the optical materials which are not necessarily needed for other methods of polymeric micro-optics fabrication. The array of issues which must be considered in optimizing an optical material formulation for micro-jet printing of microlenses are listed in **Figure 6**. Firstly, to be "microjetable" by the drop-on-demand printing process a material's rheology should be somewhat Newtonian and must be reducible in viscosity to a level of about 30 centipoise. This is typically accomplished by heating the material to the temperature required to achieve this threshold viscosity, so the optical formulation employed must also be chemically stable at that temperature. Secondly, to enable formation of printed optical elements with high precision and dimensional reproducibility, the optical material must be capable of rapid and controllable solidification. This means that the material must lend itself to *in-situ* solidification by cooling and/or UV-spot-curing, and it should, ideally, be free of solvents which can result in anisotropic shrinkage during solidification.

After printing and forming of the desired optical element, the optical material utilized must also

have that set of optical performance and durability properties needed for the particular application. These properties include the requisite index of refraction & transmissivity at the intended wavelength of use, as well a good adhesion to the substrate and the capability for handling the power levels provided by the optical irradiation sources.

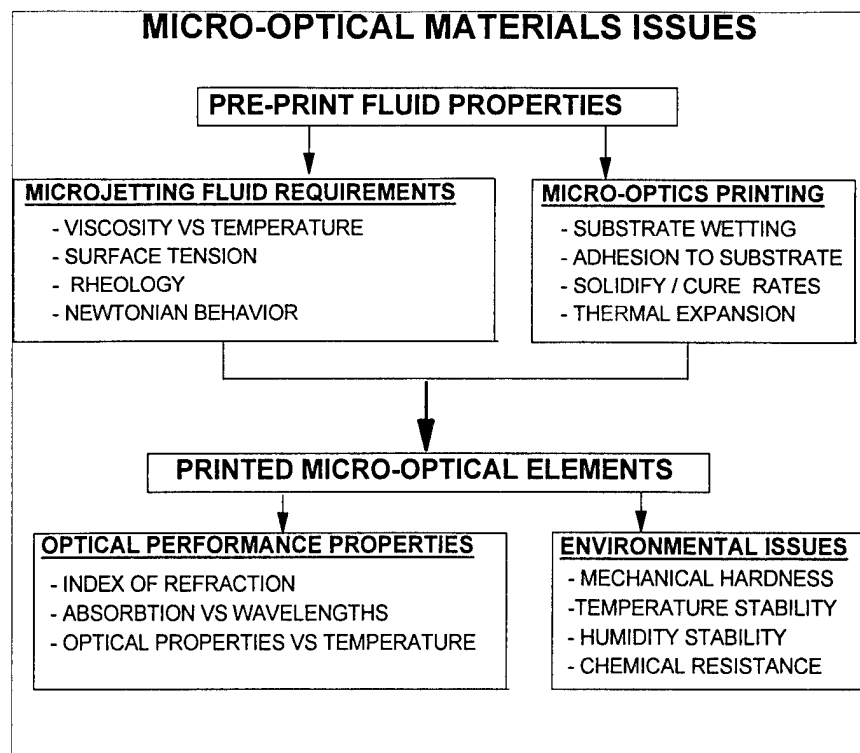


**Figure 6.** *Issues to be considered when optimizing optical material formulation properties for both micro-jet printing and printed microlens performance.*

A number of commercially available optical materials were tested which met some of above-mentioned requirements. For example, some commercially available optical adhesives and thermoplastics were used to print and form, reproducibly, micro-optical elements with good optical performance; however, these materials lacked some of the qualities, such as mechanical and temperature stability, which would be required for commercial applications. Consequently, development of *custom* optical materials which could satisfy simultaneously the printability, optical performance and durability sets of requirements was a major goal of this work.

The two classes of optical materials which have been developed here for printing of micro-optics are *UV-curing epoxy resin systems* and *higher-temperature (e.g, 200 versus 90 °C ) optical thermoplastics*. The UV-curing optical materials are preferable from a mechanical and thermal durability standpoint. In addition to supplying the requisite optical performance properties, an

ideal formulation of such material should be stable at the microjetting temperature, relatively high in viscosity at room temperature and rapidly stabilized on the target substrate by flashes of UV irradiation.

The optical materials optimization effort culminated with series of UV-curing optical formulations. These materials are easily microjettable and chemically stable (in the pre-cure state) up to 170°C. They are cured by 265 nm UV irradiation and subsequent baking at 120°C. The index of refraction may be varied in the formulation over the range 1.52-1.56 at 850 nm, and its transmissivity in the near infrared is greater than 95%.

A comparison for both hardness and adhesion on both uncoated and low-wet-coated glass substrates of two commercial optical thermoplastic materials and one of these custom UV-curing optical resins(MRX-115) is given in **Figure 7**. Here the UV-curing formulation exceeds the commercial thermoplastics in both of these properties by at least a factor-of-two. The stability of micro-optical

elements printed with this material at temperatures up to 200°C renders it suitable for relatively high-power commercial applications. This stability is demonstrated by the data of **Figure 8**. Here four microlenses printed with three different numbers of 50  $\mu\text{m}$  diameter droplets of MRX-115 were measured for focal length after baking for 1 hr at successively higher temperatures up to 200°C. The

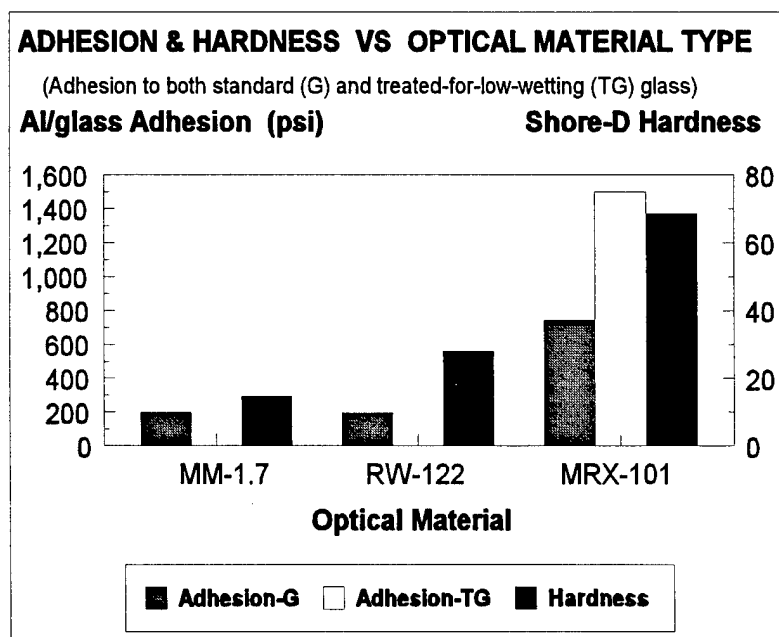


**Figure 7.** Comparison for adhesion to untreated (G) and low-wetting glass (TG) and for hardness of 2 thermoplastic (MM-1.7 & RW-122) and a UV-curing resin (MRX-101).

variations of the average focal lengths of these lenses with thermal cycling were found to be within the range of measurement error, indicating that microlenses printed with this material could endure such temperatures in subsequent processing or operation without significant degradation in optical properties.

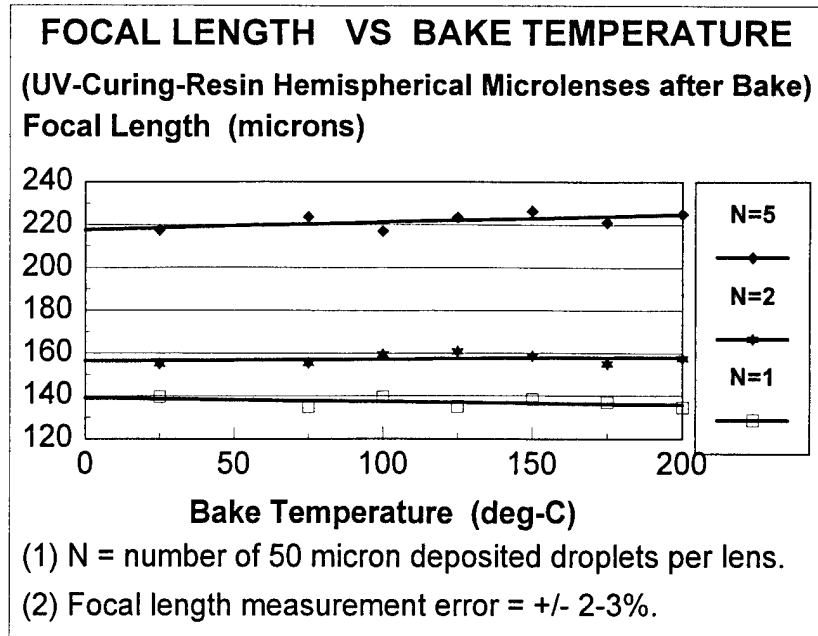


**Figure 8.** Focal length of three sizes of microlenses printed with MRX-115, after bakes at temperatures up to 200 °C, where variation is within measure error.

### 3.3 PRINTING METHODOLOGY

In our drop-on-demand microjet printing of micro-optical elements, a microdroplet of optical material is dispensed, at a typical velocity of 2-4 m/s, onto a target substrate surface 0.5-1 mm from the device nozzle. Upon striking an optical substrate a droplet spreads, coalesces with other droplets and is solidified by cooling and curing to form a microlens of the desired dimensional and optical characteristics.

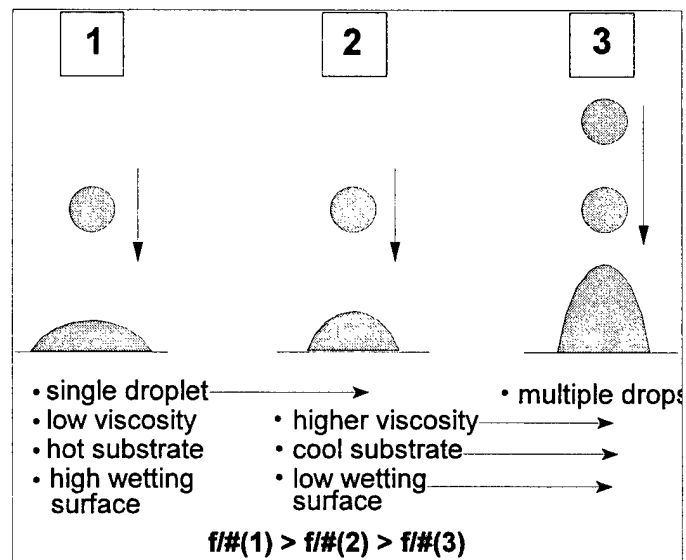


**Figure 9.** Variation of circular-footprint printed microlens aspect ratio by varying process parameters.



A plano/convex microlens having a *circular* "footprint" on its substrate is formed by printing one or more droplets at a single target site. The size and speed ( $f/\# = \text{focal-length/diameter}$ ) of the printed microlens may be adjusted independently by varying a number of parameters, such as the size and number of droplets, along with the temperature and wettability of the substrate surface, as illustrated in **Figure 9**. For example, decreasing the substrate temperature and/or increasing the viscosity of the fluid being dispensed will reduce the spread of deposited droplets prior to solidification, thereby increasing the aspect ratio of a lenslet printed with a fixed volume of material. Printed microlens aspect ratios may alternatively be increased by applying an optical coating to the target substrate which reduces its wettability (i.e., increases droplet contact angle) by the deposited material.<sup>18</sup>

An *anamorphic* plano/convex microlens, e.g., one having a non-circular "footprint" on its substrate surface, is formed by printing a pattern of *adjacent* droplets and controlling their center-to-center spacings and rate of solidification to obtain an element of the desired configuration and dimensions. In this case the differential temperature between print head and substrate is also critical, but the target surface must be sufficiently wetting to the material being printed to enable the coalescing of nearest-neighbor droplets prior to solidification.<sup>19,20</sup>

The process for printing any microlens or an array of microlenses is entirely data driven. A micro-optics printing process sequence typically runs as follows:

- (1) adjust print head parameters for selected optical material (orifice diameter, temp., drive waveform, etc.);
- (2) prepare target substrate surface (cleanliness, treatments for wettability & adhesion);
- (3) print pattern of droplets at substrate lenslet site (1 or more at common or adjacent positions);
- (4) allow droplets to coalesce into uniform lenslet (of design shape & size);
- (5) solidify lenslet by cooling and/or UV-curing
- (6) apply any post-print processes (bake for final cure or overcoat for anti-reflection).

The process variables utilized are:

- (1) Type & properties (viscosity and surface tension) of optical materials;
- (2) Print head reservoir & device temperatures (25-240°C);
- (3) Device driving waveform (pulse height & shape, frequency);
- (4) Orifice diameter (25-70  $\mu\text{m}$ );
- (5) Substrate temperature (10-100°C);
- (6) Substrate surface treatment (cleaning, coatings);
- (7) Curing process, e.g., UV-expose algorithm (sequencing, irradiation on time, intensity).

## 4.0 PRINTED MICROLENSSES

### 4.1 CIRCULAR FOOTPRINT MICROLENSSES

#### 4.1.1 Spherical Microlenses

Circular-"footprint", spherical, microlenses are defined here as plano/convex lenslets having a circular area of contact with the supporting substrate and a circular-arc profile perpendicular to the substrate surface. An example of printed microlenses of this type is shown in **Figure 10**, which consists of photos of the

substrate-plane and far-field diffraction pattern of a 50 x 50 array of 100  $\mu\text{m}$  diameter hemispherical microlenses on 125  $\mu\text{m}$  centers, each printed with a single 50  $\mu\text{m}$  droplet of a UV-curing optical material.

Here the array is illuminated from behind the substrate with

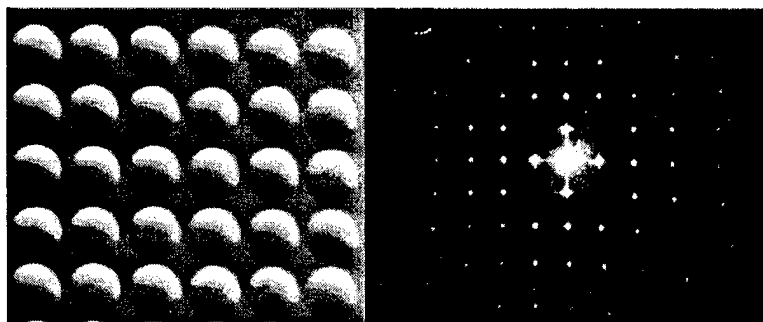


**Figure 10.** Array (left) and far-field diffraction pattern (right) of 100  $\mu\text{m}$  diameter hemispherical microlenses printed on 125  $\mu\text{m}$  centers with UV-curing optical material onto low-wetting glass.

632.8 nm collimated light, and the symmetry and clarity of the diffraction pattern are indicative of the uniformity in shape and spacing of the printed lenslets.

As the number of droplets deposited per site (N) is increased, the diameters and focal lengths of the printed microlenses are correspondingly increased, as illustrated by the data of **Figures 11 & 12**. For both parameters the rise in value with increasing N-number is approximately logarithmic. A low-wetting coating applied to the glass reduces the spread of material prior to solidification, resulting in both smaller diameters and focal lengths for the same number of deposited droplets. The effect of the reduced spreading of the material on the coated substrate is to increase the height-to-width aspect ratio and reduce the radii of curvature of the printed

lenslets, which results in a greater proportional decrease in focal length than diameter.

For the UV-curing optical materials used here the primary variable in determining the lenslet aspect ratio achieved with a given number of deposited droplets is the wettability of the substrate surface to the material. This is due to the fact that these materials are not completely solidified at room temperature and will continue to flow over time until stabilized by UV irradiation. This flow may be arrested by spot curing each lenslet *in situ* within a few seconds of deposition, but this impacts adversely the time required for printing a microlens array. On the other hand, for optical thermoplastics which are solid at room temperature, the key variable in determining the aspect ratio of a hemispherical microlens of given volume is the rate

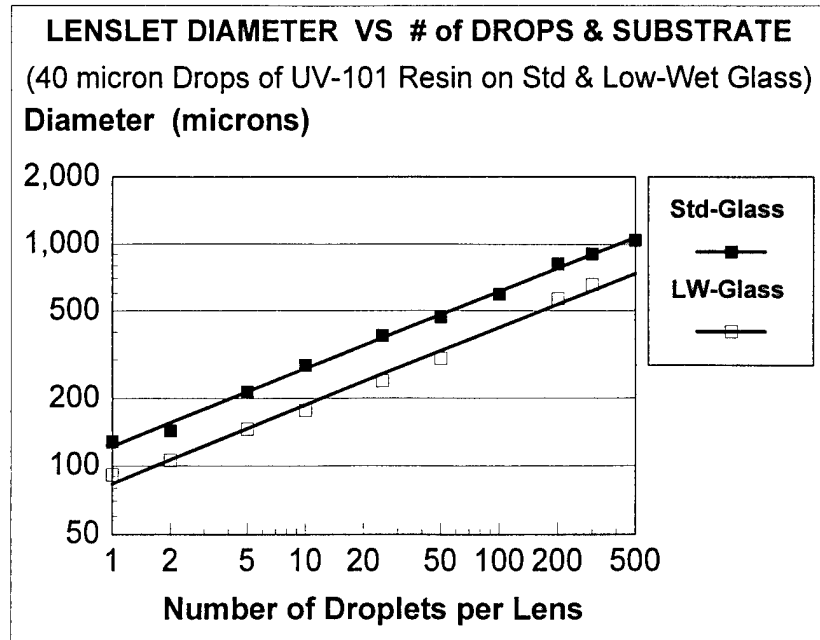


**Figure 11.** Increase in lenslet diameter with number of 40  $\mu\text{m}$  droplets of UV-curing material deposited onto untreated (Std) and low-wet-treated (LW) glass.

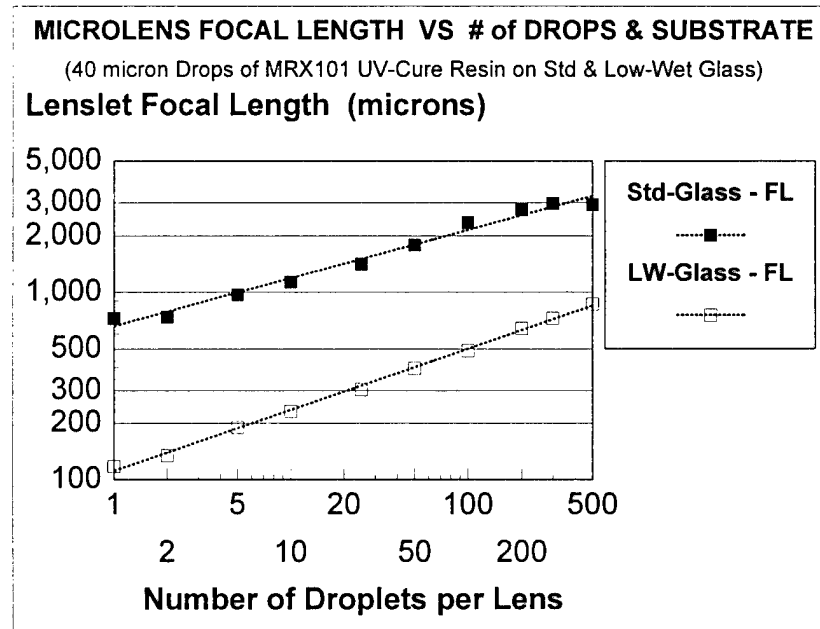


**Figure 12.** Increase in focal length with number of 40  $\mu\text{m}$  droplets of UV-curing material deposited onto untreated (Std) and low-wet-treated (LW) glass.

at which it solidifies upon impact with the substrate, which, in turn depends upon the temperature differential between the material before impact and the substrate.

These effects are illustrated by the data of **Figure 13**, which show the variations of lenslet focal lengths with diameters for a UV-curing material deposited onto untreated and low-wet-treated glass and for a high softening point optical

thermoplastic on untreated glass. Here printed microlens speeds ( $f/\#$ ), given by the slopes of the curves, are typically *constant* over a wide range of diameters for each UV-curing material printed onto low-wetting glass and cured after printing all of the lenslets in the series, as they are for optical thermoplastics printed onto any substrate surface. On the other hand, the speeds of UV-curing lenslets printed onto more wetting surfaces tend to decrease as the volume of deposited material increases.

An example of utilizing substrate temperature to determine printed spherical microlens aspect ratio is shown in **Figure 14**. The four lenslets here

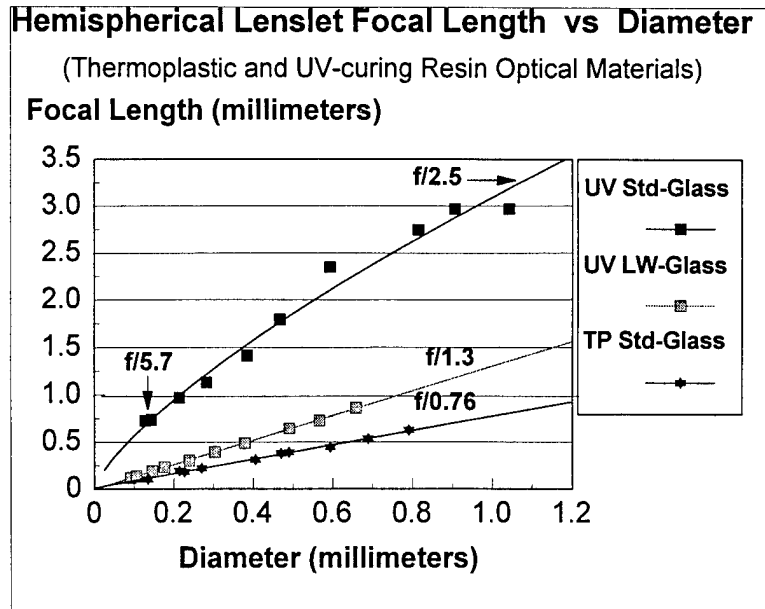


**Figure 13.** Variation of microlens focal length with diameter for UV-cure material on untreated (Std) & low-wetting glass and for a high-temperature thermoplastic on untreated glass.

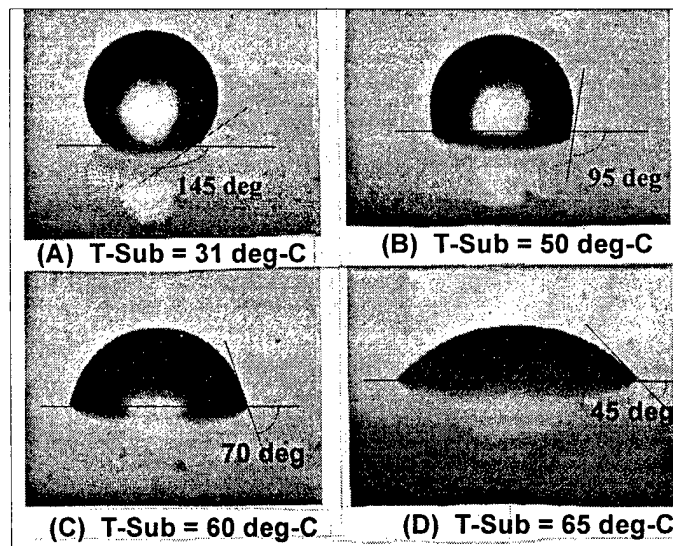


**Figure 14.** Four microlenses printed with equal volumes of optical thermoplastic at 215 °C onto substrates at four different temperatures.

were all printed with bursts of 15 each 50  $\mu\text{m}$  diameter droplets of an optical thermoplastic dispensed at a temperature of 215°C and at a rate of 2,000 droplets per second. The resulting height/width aspect ratio and surface contact angle of each microlens depends upon the speed of cooling & solidification, which is a sensitive function of the differential temperature between print head and substrate. It should be noted here that the fabrication of microlenses with substrate surface contact angles greater than 90°, as in Fig. 14-A&B, cannot be readily achieved by the more conventional approaches mentioned above.

To maximize the fill factor for a rectilinear array of printed microlenses one can utilize the UV-curing optical materials and the Shuttle stage of the Micro-optics Printing Station to flash-cure each lenslet within seconds after deposition, thereby enabling the reduction of the edge-to-edge distances to nearly zero without incurring any running together of adjacent lenslets. This method was employed in printing the array pictured in **Figure 15**, showing 950  $\mu\text{m}$  diameter hemispherical microlenses on 1 mm centers. Here each lenslet was formed by depositing 283 each 60  $\mu\text{m}$  droplets and spot curing within 10 sec.

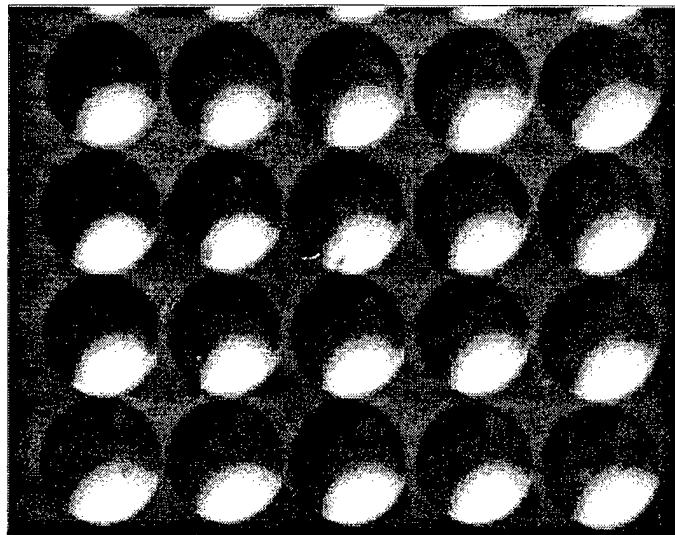


**Figure 15.** *High-fill-factor array of 950  $\mu\text{m}$  hemispherical microlenses, each printed with UV-curing material and flash-cured immediately after its deposition.*

#### 4.1.2 Hyperbolic Microlenses

*Hyperbolic* circular-"footprint"-microlenses are defined here, again, for the purpose of comparison, as those having a circular contact area with the supporting substrate, but with non-circular, nearly-hyperbolic profile perpendicular to the substrate. Such microlens configurations

may only be printed with the UV-curing optical materials, where intervening spot-cures during printing of a lenslet are used to arrest the flow of material on the substrate and allow creation of relatively large height/diameter aspect ratios.

An example of a printed microlens with hyperbolic profile is shown in **Figure 16-A**. It was printed by dispensing a total of 25 droplets of UV-curing material, in 5 each 5-droplet bursts at 2 kHz, at the same print site, where the Shuttle Stage was utilized to move the UV light pipe port over the print site for a 0.2 sec flash of irradiation at the end of each burst. The spherical lenslet of identical volume (Fig. 4-B) was cured only after deposition of all 25 droplets, so its diameter and focal lengths are 40% and 80% larger, respectively, than the higher aspect ratio one.

The process of incrementally building lenslet aspect ratio by this method is illustrated in **Figures 17 & 18**, where

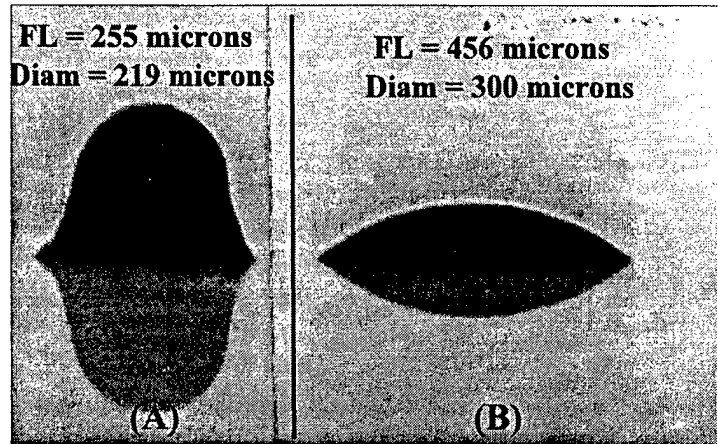


**Figure 16.** Profiles of (A) quasi-hyperbolic and (B) spherical microlenses printed with 25 each 40  $\mu\text{m}$  droplets of UV-cure material using 5 each 0.2 sec UV-flashes during and 1 after printing.

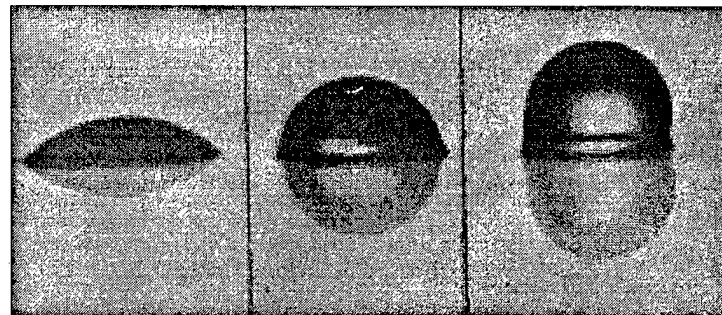


**Figure 17.** Microlenses at 150X magnification, printed with (left-to-right) 5, 7 & 9 each 50 $\mu\text{m}$  droplets of MRX-110B uv-curing resin, with automated spot cures after each droplet deposition.

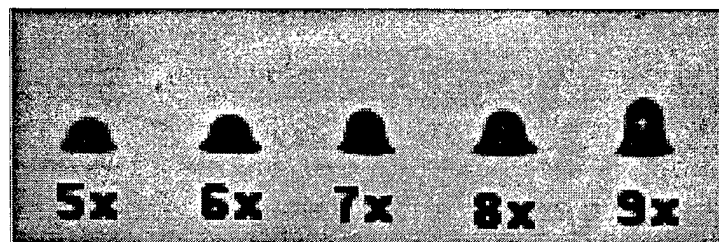


**Figure 18.** Increasing printed microlens aspect ratio by repeating cycles of UV spot-curing after deposition of each 50  $\mu\text{m}$  droplet, from 5 to 9 times (left-to right).

an intervening spot cure was applied after the printing of each droplet. Here the total cycle time for printing and spot curing each deposition is over 30 sec, with the speed limiting factor being the time required for the irradiated material to stabilize prior to the next deposition.

#### 4.1.3 Microlenses Printed onto Optical Fibers

Methods involving etching and/or micro machining of the tips of optical fibers<sup>21</sup> have been employed to increase their effective numerical apertures for receiving light from sources such as diode lasers. Alternatively, spherical microlenses may also be printed directly onto the flat, polished tips of the fibers,<sup>22</sup> as illustrated in **Figure 19**.

Here a v-groove chuck was used to position each fiber with flat polished tip in the substrate plane, and the targeting microscope was utilized to locate the print along the fiber axis. Since the edge of the fiber tip constrains the flow of deposited material prior to solidification/curing, the curvature of the printed

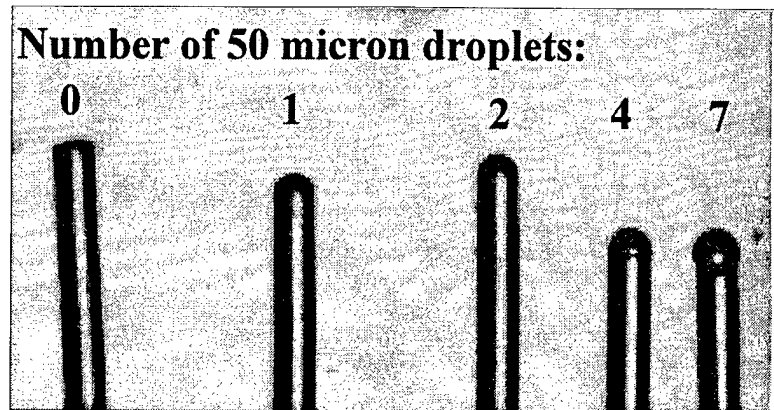


**Figure 19.** 140  $\mu\text{m}$  diameter optical fibers with printed microlenses of decreasing radii of curvature as the number of deposited droplets is increased (left-to-right).

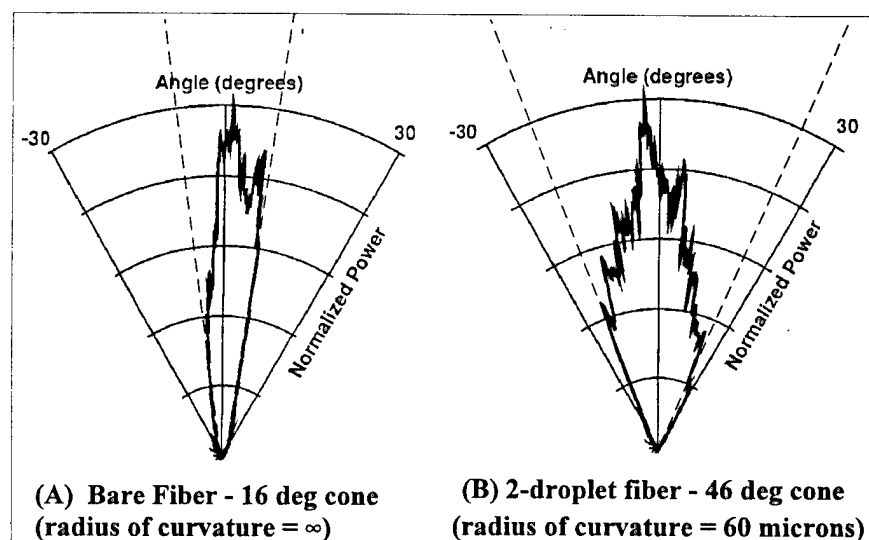


**Figure 20.** Angular distribution of normalized power emitted from flat (A) and lensed (B) fiber tips.



lenslet may be incrementally controlled according to number and size of deposited microdroplets. These microlenses were printed at 145 °C with an optical thermoplastic which has a substantially higher index of refraction (1.70) than the fibers (1.53). To measure the effect of the printed lenslets on their tips a HeNe laser was coupled into the back ends of the fibers, and a power meter and pin hole system were used to measure the angular power distribution of the emitted irradiation. The data given in **Figure 20** for the normalized power in one plane demonstrate how the application of two 50  $\mu\text{m}$  droplets to a fiber tip increased the light divergence angle by a factor of three over that obtained with a flat-tipped fiber, which translates into a 3x increase in numerical aperture for the fiber. The printing of such lenslets could be used to increase the efficiency of coupling of power from a diode laser into an optical fiber.

#### 4.1.4 Microlens Arrays for Reflectors

Another potential application for printed hemispherical microlenses is arrays for "cat's eye" reflectors (which have arrays of differently sized lenses on both sides of the same substrate, one with a highly reflective coating) for interferometric tracking<sup>23</sup> and air-borne communications. Investigation of the potential suitability of utilizing microjet printing for fabrication of cat's eye reflectors began near the end of this contract. It was

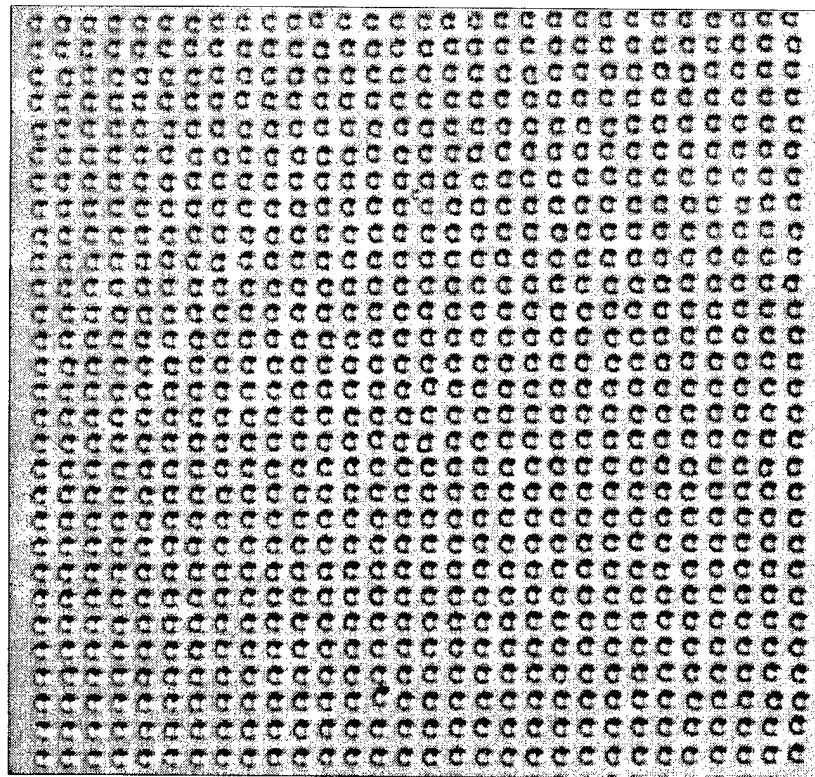


**Figure 21.** 30 X 30 array of 154  $\mu\text{m}$  diameter MRX-115 microlenses printed onto C6-treated cover glass on 197  $\mu\text{m}$  centers, where back focal lengths have been adjusted (by number of 50  $\mu\text{m}$  droplets deposited at each site) to be at backside of substrate.

started by printing single arrays of hemispherical microlenses onto glass slides and adjusting back focal lengths to be exactly at the back surface of the substrate.

An example of the “half cat’s eye” reflector arrays printed for testing at the Phillips Lab is given in the photos of **Figures 21 & 22**. Here the number of 50  $\mu\text{m}$  droplets deposited at each lenslet site was adjusted to get the back focal lengths at the backside of the 150  $\mu\text{m}$  thick cover glass slides. The slides, pre-treated with low wetting material, were then baked at 120°C for an hour after printing and UV-curing of the microlenses. The focal lengths were measured using light entering from the lenslet side of the substrate and locating the position of the plane where the aperture of the condenser lens is most clearly imaged by each lens.

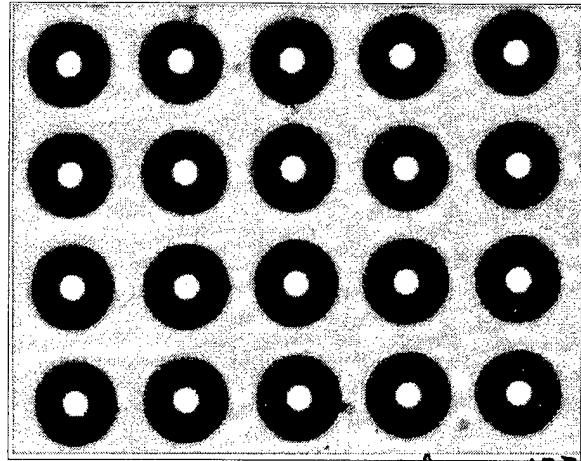


**Figure 22.** *Portion of above microlens array shown focusing an aperture image at backside of substrate with illumination from top of microlenses.*

Initial data taken at the Phillips Lab with a mirror at the back substrate surface indicated focused reflection values greater than 10%, suggesting that reflector fabrication may be a good potential application for microlens printing technology.

## 4.2 ANAMORPHIC MICROLENSES

### 4.2.1 Elliptical Microlenses

One type of microjet printable *anamorphic* plano/convex microlens, e.g., one having a non-circular "footprint" on its substrate surface, has a hemi-ellipsoidal shape. Such lenslets, formed by printing a line of adjacent droplets which coalesce on the substrate prior to solidification, have the potentially useful optical characteristic of providing two different focal lengths.

An example of printed "hemi-elliptical" microlenses is given in **Figure 23**, where photos of four lenslets are shown in three different planes - at the substrate and at two heights above it. Each of these microlenses was printed by depositing six each 35  $\mu\text{m}$  diameter droplets of optical thermoplastic at

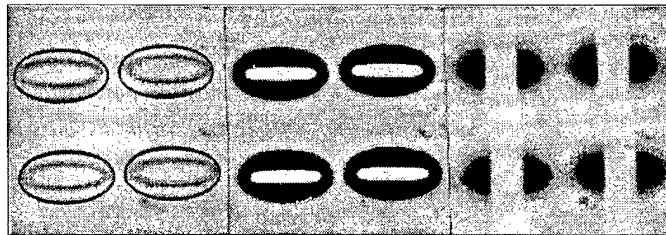


**Figure 23.** Four each hemi-elliptical microlenses,  $284\mu\text{m} \times 146\mu\text{m} \times 20\mu\text{m}$  high, viewed in substrate plane (left), "fast" ( $f/1.5$ ) focal plane (middle) and "slow" ( $f/3.2$ ) focal plane (right).

150°C onto 40°C untreated glass on 40  $\mu\text{m}$  centers along the major axis direction. As the collimated light from behind the substrate passes through these lenslets it is first brought to a line focus parallel to the major axis at the "fast" focal length due to the curvature about the minor axis. Moving further away from the substrate the light is brought to a second, perpendicular line focus at the "slow" focal length due to the much more gradual curvature about the major axis.

The primary result of increasing the spacing between deposited droplets is to increase the length of the major axis and the radius of curvature along that axis, thereby increasing the "slow" focal length in that plane. To demonstrate this, a series of arrays hemi-elliptical microlenses was made by printing six 60  $\mu\text{m}$  droplets of optical thermoplastic ( $n_d = 1.704$ ) at 150°C onto untreated glass at 40°C, on center-to-center spacings over a 30-75  $\mu\text{m}$  range. Portions of two of those arrays, with

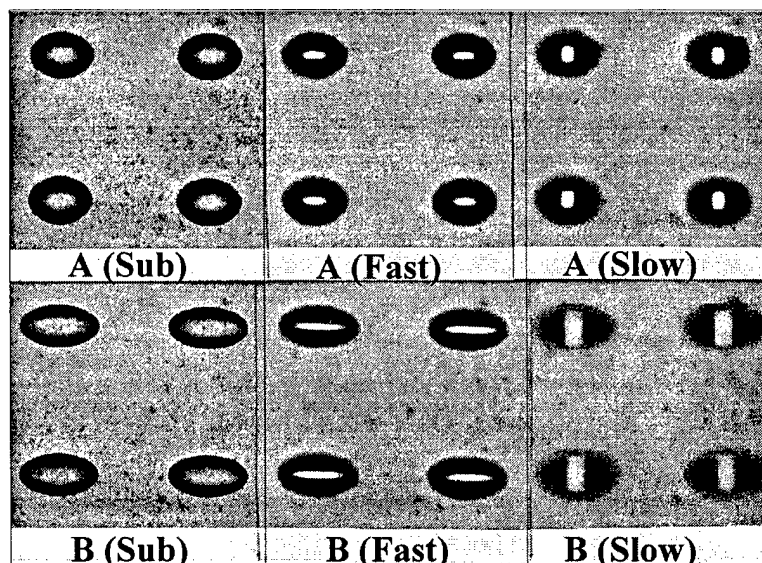


**Figure 24.** Two arrays of 4 each hemi-elliptical microlenses printed with 6 each 60  $\mu\text{m}$  droplets of optical thermoplastic on (A) 50  $\mu\text{m}$  & (B) 67  $\mu\text{m}$  centers, shown in (L->R) substrate, "fast" [FL: (A)=432 $\mu\text{m}$ , (B)=362 $\mu\text{m}$ ] and "slow" [FL: (A)=900 $\mu\text{m}$ , (B)=1,543 $\mu\text{m}$ ] focal planes.

microlens droplet spacings of 50  $\mu\text{m}$  and 67  $\mu\text{m}$ , are shown in **Figure 24**. Again, each array is viewed at the substrate surface and in the “fast” and “slow” focal planes. Here an increase in droplet spacing of only 17  $\mu\text{m}$  raised the “slow” focal length by 83% (from 900  $\mu\text{m}$  to 1,643  $\mu\text{m}$ ) but reduced the “fast” focal length by only 16% (from 432  $\mu\text{m}$  to 362  $\mu\text{m}$ ).

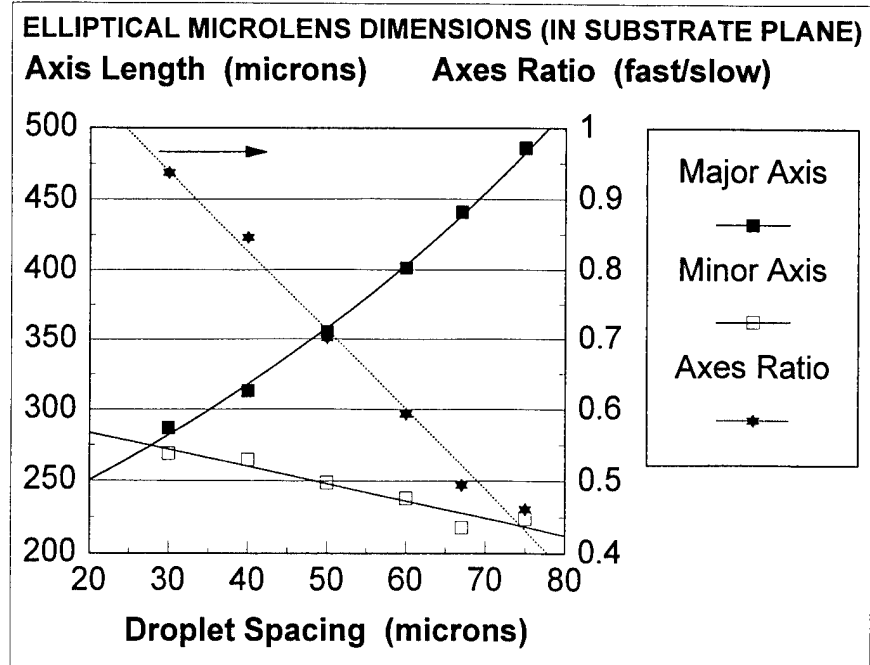


**Figure 25.** Variation of hemi-elliptical microlens axes and axis ratio (width/length) in substrate plane with spacings of 6 deposited 60  $\mu\text{m}$  droplets.

The dependence of measured axial dimensions for six arrays of this series of hemi-elliptical microlens is indicated in **Figure 25**. Each data point is the average value for three lenslets selected at random from each array, where the standard deviation in each case was less than 1%. At a droplet spacing of 30  $\mu\text{m}$  the lenslets are 287  $\mu\text{m}$  long and nearly hemispherical (axis ratio  $\sim 1$ ), while a spacing of 75  $\mu\text{m}$

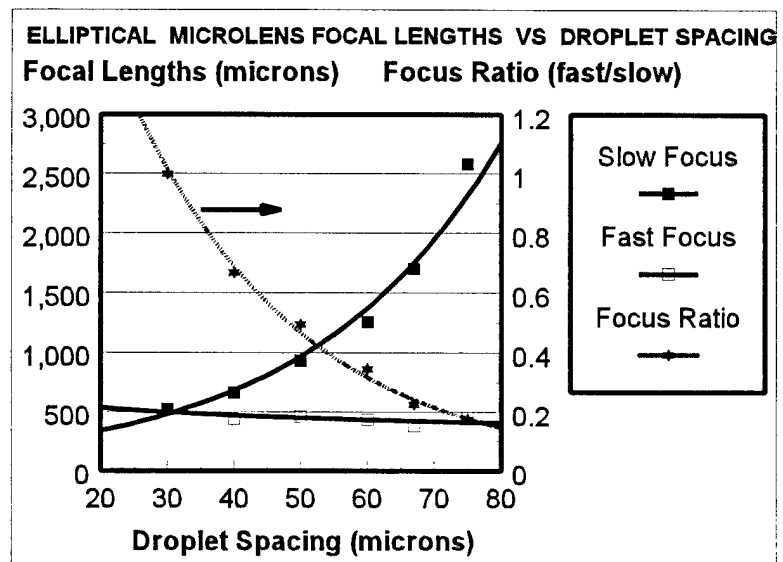


**Figure 26.** Variation of hemi-elliptical microlens focal lengths and focal length ratio with spacing of 6 deposited 60  $\mu\text{m}$  droplets.

produces 486  $\mu\text{m}$  long hemi-elliptical microlenses with major axis length exceeding that of the minor axis by a factor-of-two. It can also be seen that the rate of increase of major axis length with increasing droplet spacing is much greater than the rate of minor axis decrease, resulting in a steep drop in fast/slow/ axes ratio.

The dependencies of measured focal lengths for microlenses from these arrays, as shown in **Figure 26**, reflect those of the corresponding lenslet dimensions. As droplet spacing is increased the major axis curvature increases rapidly, resulting in a factor-of five rise in the “slow” focal length (from 521  $\mu\text{m}$  to 2.58 mm), while the “fast” focal length drops over this range by only 13%, enabling a 5.7X drop in focal length ratio. The lengths and focal ratios of hemi-elliptical microlenses may also be raised by increasing the number of deposited droplets, as shown in **Figure 27** for two 500  $\mu\text{m}$  X 200  $\mu\text{m}$  X 42  $\mu\text{m}$  hemi-elliptical microlenses printed with 10 each 60  $\mu\text{m}$  droplets and having "fast" and "slow" focal lengths of FL=190  $\mu\text{m}$  and 1.67 mm, respectively.

Increasing further either the number of droplets printed per lens or their spacing will result in blurring the slow focus as the major axis curvature first flattens and then starts to sag in the middle.

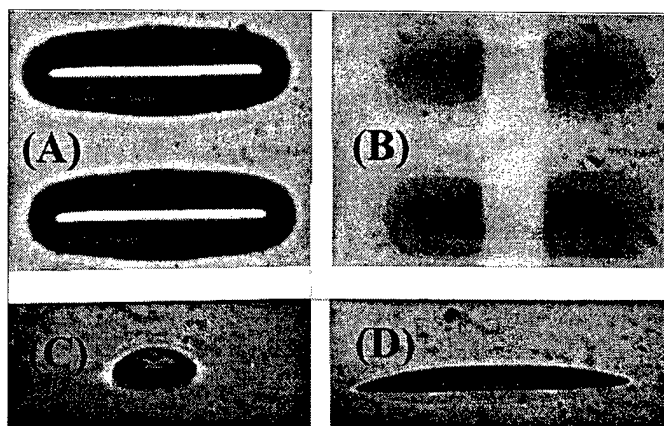


**Figure 27.** Two hemi-elliptical microlenses printed with 10 each 60  $\mu\text{m}$  droplets of optical thermoplastic on 50  $\mu\text{m}$  centers, shown in (A) “fast” and (B) focal planes and in profile along (C) minor and (D) major axis.

Additional series of hemi-elliptical microlenses were also printed with optical thermoplastics of differing refractive indices, higher melting points (e.g., printed at 175°C versus 150°C) and with multiple droplets per site, which altered magnitudes and slopes but not the fundamental functional relationships of these parameters. The use of different numbers of differently sized droplets printed per site, as well as the number and spacings of the sites, enables the independent

adjustment of printed hemi-elliptical microlens dimensions and focal length ratios.

Printing hemi-elliptical microlenses with UV-curing optical materials require modifications of the procedures used above for optical thermoplastics, because the UV material have lower surface tension and, in addition, do not solidify until exposed to the irradiation. The modification involves altering the sequence of droplet deposition (e.g., site #1,3,5,2,4 & 6) and providing precise time intervals between completion of the printing of a lenslet and initiation of the *in-situ* UV-spot-curing. An example of

UV-cured hemi-elliptical

microlenses is given in **Figure 28**.

Here lenslets with length/width

aspect ratios varying over the range

1-4 were printed by increasing the

center-to-center spacings of the six

droplets (deposited along the

vertical direction) from 25  $\mu\text{m}$  to

95  $\mu\text{m}$ . In this case all eight

lenslets were exposed to 10

seconds of UV irradiation and

then baked at 120°C for an

hour.

The dimensional and focal lengths measured for the lenslets shown in **Figure 28** are plotted in **Figure 29** as functions of center-to-center droplet spacings. It can be seen that these data are quite similar

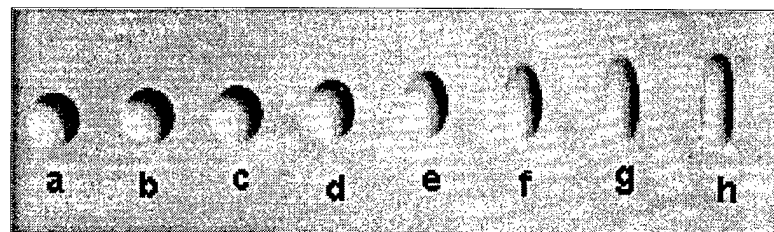


**Figure 28.** Hemi-elliptical microlenses printed with 6 each 60  $\mu\text{m}$  droplets of UV-curing optical material in the vertical direction on center-to-center spacings varying in increments of 10  $\mu\text{m}$  from (a) 25  $\mu\text{m}$  to (h) 95  $\mu\text{m}$ .

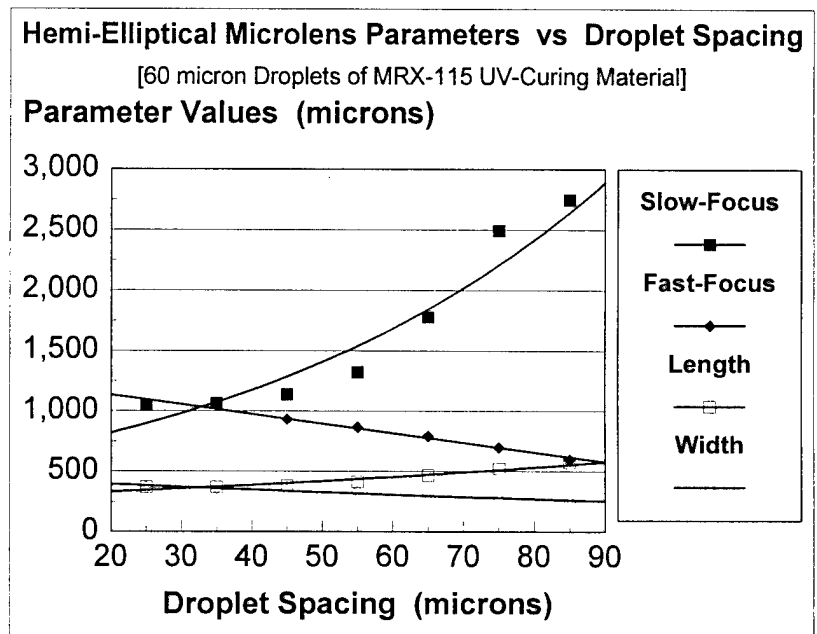


**Figure 29.** Variation with droplet spacing of focal lengths and dimensions of hemi-elliptical lenslets of Fig. 28.

to those obtained for hemi-elliptical microlenses printed with optical thermoplastics. Unlike the thermoplastics, however, the UV-cured lenslets have the thermal and mechanical durability needed for applications requiring higher power handling capacity and the capability to survive subsequent high-temperature processing steps.

Another methodology for fine-tuning the geometry of printed hemi-elliptical microlenses is to select a comparatively large site-to-site distance and then vary the number of droplets deposited at each site. This fixed site stepping distance must be selected so that the minimum number of droplets to be deposited per site provides sufficient material volume to allow adjacent deposits to coalesce.

To test this approach the MRX-115 UV-resin material was used to print a series of such lenslets by depositing multiple droplets at

adjacent target sites and measuring their dimensions and focal lengths. Numbers of 50  $\mu\text{m}$  droplets ranging from 10 to 300 were printed at each of 6 sites located on 125  $\mu\text{m}$  centers, then UV-cured after completion of the depositions for each lenslet. In the seven representative microlenses shown in **Figure 30** (each

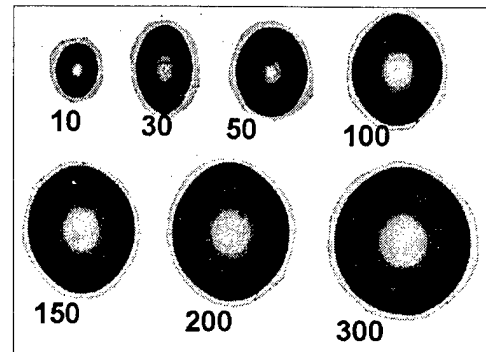


**Figure 30.** Hemi-elliptical microlenses at 60X magnification, printed by depositing indicated number of 50  $\mu\text{m}$  droplets of MRX-115 at 6 sites on 125  $\mu\text{m}$  centers.

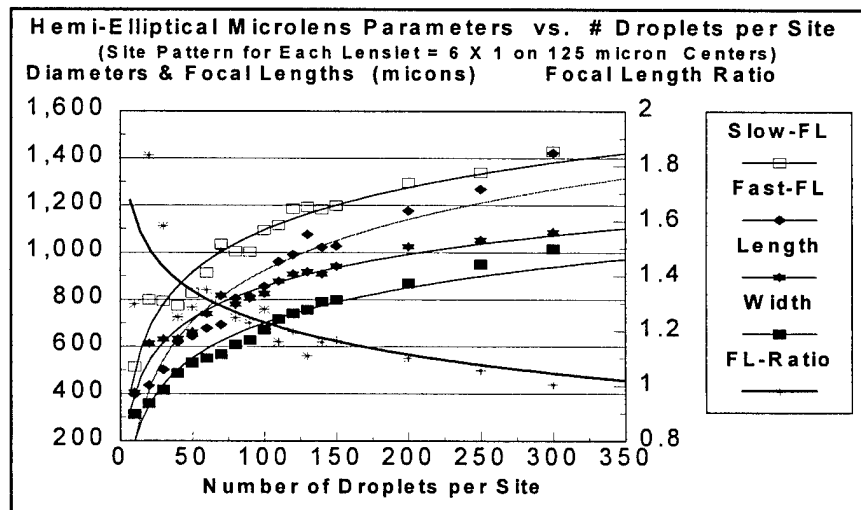


**Figure 31.** Variation of dimensions in substrate plane and fast and slow focal lengths (left scale), along with focal length ratio (right scale), of printed hemi-elliptical lenslets, with number of 50  $\mu\text{m}$  droplets deposited at each of six sites on 125  $\mu\text{m}$  centers.

cut from one photo and pasted as a group) it can be seen how the length-to-width aspect ratio varies inversely with the number of droplets per site. Data for the variation of the substrate-plane dimensions, focal lengths and focal length ratio (slow/fast) with droplet number are plotted in **Figure 31**. As dimensions and focal lengths increase with droplet number the lenslets evolve from distinctly elliptical to nearly spherical (slow-focal-length / fast-focal-length  $\approx 1$ ).

#### 4.2.2 Cylindrical, Square and Rectangular Microlenses

As droplet center-to-center distance is increased in the printing of hemi-elliptical microlenses, the radius of curvature about the major axis increases until the surface in that plane flattens (focal length= $\infty$ ).

This “critical” spacing varies with droplet size, the properties of the optical material and the condition of the substrate surface. By increasing the number of deposited droplets, arrays of hemi-cylindrical microlenses may be printed for applications such as collimating only the rapidly diverging plane of light from stripes of edge-emitting diode laser bars,

which. An example of such an array made by printing 50  $\mu\text{m}$  droplets of optical thermoplastic at 150°C on 70  $\mu\text{m}$  centers onto 40°C glass is shown in **Figure 32** (again under collimated back-lighting).

By extending the step-and-repeat deposition of microdroplets in two

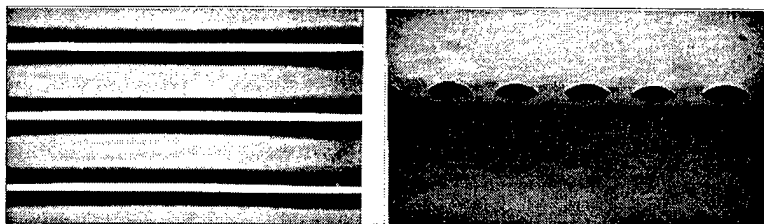


**Figure 32.** 165  $\mu\text{m}$  wide, 37  $\mu\text{m}$  high, printed cylindrical microlenses shown in (left) focal plane and (right) in profile, where focal length is 215  $\mu\text{m}$  ( $f/1.3$ ).

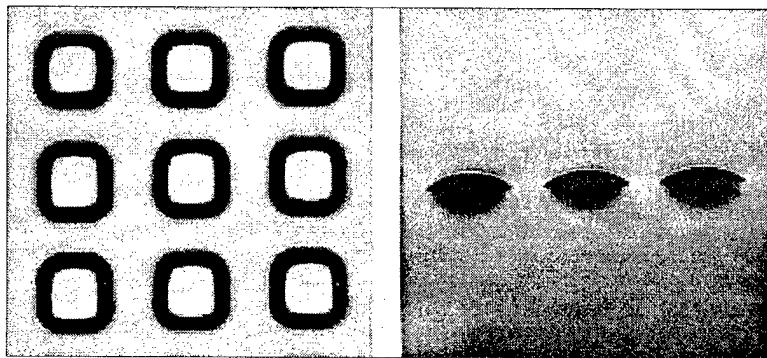


**Figure 33.** Array of 300  $\mu\text{m}$  square, 50  $\mu\text{m}$  high optical thermoplastic microlenses printed on 400  $\mu\text{m}$  centers shown in (left) focal plane ( $FL=227 \mu\text{m}$ ) and (right) in profile.



directions, arrays of nearly square and nearly rectangular microlenses may be printed for potential use in optimization of fill factor for specialized light collection applications (e.g., CCD pixel sensitivity enhancement). For example, an array of square microlenses with domed tops, shown in **Figure 33**, was fabricated by printing 4X4 patterns with the same process utilized for the cylindrical lenslets of Figure 29. Note that the measured focal length ( $227\text{ }\mu\text{m}$ ) of these square lenslets gives (using substrate plane lenslet width of  $300\text{ }\mu\text{m}$  as aperture value) a very fast  $f/0.76$  speed.

Fabricating arrays of nearly rectangular microlenses involves only extending the number of deposited droplets to achieve target dimensions.. For example the lenslets shown in **Figure 34** were made using the same printing process but depositing a 4X12 droplet pattern.

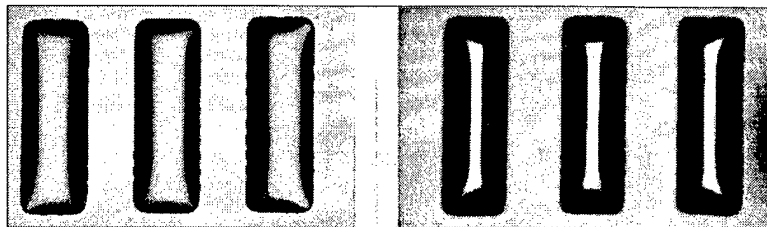


**Figure 34.** Array of  $300\text{ }\mu\text{m} \times 870\text{ }\mu\text{m}$  rectangular lenslets on  $500\text{ }\mu\text{m}$  centers shown in (left) substrate and (right) focal ( $FL=375\text{ }\mu\text{m}$ ) planes.

## 5.0 DIODE LASER COLLIMATION

### 5.1 ADVANTAGES OF PRINTED MICROLENSES

We have shown that by adjusting the size, number and spacing of deposited droplets of optical material printed hemi-elliptical microlenses may be "tailored" to achieve both the dimensional and focusing specifications required for a particular application, such as collimating the individual beamlets from edge-emitting diode laser arrays. The concept of this application, as illustrated in **Figure 35**, involves using an array of printed microlenses to collimate the anisotropically diverging outputs from the emitters, in a "one-on-one" basis. A single macrolens would then be used to focus the collimated beamlets into an optical fiber. Here the "slow"/"fast" focal ratio would be adjusted to bring both the rapidly and more slowly divergent planes of light from the emitters to minimum area spots (waists) in the same plane, thereby providing collimation and astigmatism correction. The distance of the lenslet array from the laser array, along with the microlens major axis

lengths, would have to be scaled to capture all of emitted power from each emitter before the emerging beamlets cross each other.

In addition to providing collimation and astigmatism correction, the use of printed hemi-elliptical microlenses can make an additional contribution to the efficiency of geometric

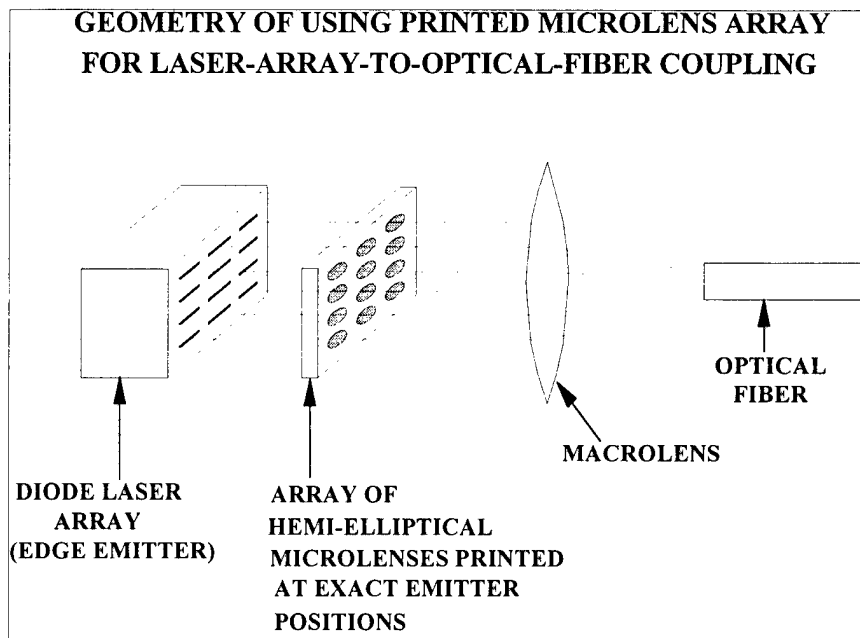


**Figure 35.** *Illustration of potential use of custom-printed array of hemi-elliptical microlenses in collimating the diverging outputs of an edge emitter diode laser arrays to maximize efficiency of geometric multiplexing into a fiber.*

multiplexing in this application. Since microjet printing is a data-driven process a custom lenslet array pattern could be printed to align with that of each individual laser array. This could be done actively by positioning an optical substrate (anti-reflection coated on both sides) at the appropriate distance from the diode laser and using a vision system to print a microlens at the center of each transmitted spot. Alternatively, an emitter map could first be made photographically, and then the coordinates of each emitter could be located with a vision system and the microlens array printed to input data.. The use of custom printed microlens arrays in this way could compensate for laseremitter registration errors caused by manufacturing variances such as laser-bar "tilt" / "smile."<sup>1</sup>

## 5.2 MICROLENS PLACEMENT ALONG BEAM AXIS

An initial experiment was performed to confirm that elimination (or reversal) of the divergence of an edge emitting diode laser with a plano/convex microlens oriented with curvature along the direction of propagation, requires locating the lenslet axially such that the effective emission points of the laser are within the

back focal length of the lenslet, as illustrated in **Figure 36**. Here

a hemispherical microlens printed on a treated cover glass, with diameter and focal length of 1,188  $\mu\text{m}$  and 1,417  $\mu\text{m}$ , respectively, was located on a z-axis translator near the facet of a visible diode laser source (LN9R05M by Matshushita Electronics Corporation, where the 670 nm

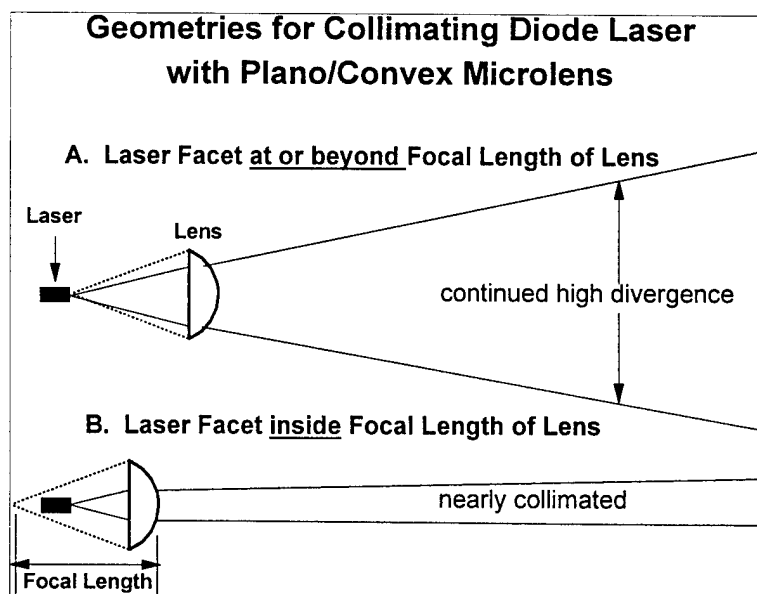


**Figure 36.** *Illustration of axial positioning optimization for edge-emitting diode laser collimation.*

<sup>1</sup>. C. Moeller, Private communication, Phillips Labs, Kirtland AFB, 1994.

radiation has horizontal and perpendicular divergence angles of  $8^\circ$  and  $30^\circ$ , respectively, with nominal astigmatism  $\leq 10 \mu\text{m}$ ). The spot size of the transmitted beam was observed on a screen as the microlens was translated away from the laser.

Microlens positional data, plotted in **Figure 37**, were obtained by

replacing the screen with a beam profiler to obtain power peaks in the parallel and perpendicular

planes of the diode laser, at a series of lenslet positions within its back focal length. The divergence angles at each lenslet position was then calculated by dividing the FWHM value by the microlens focal length. The minimums in these two curves give the optimal lenslet positions for independent collimation of the two laser emitting planes with this particular microlens.

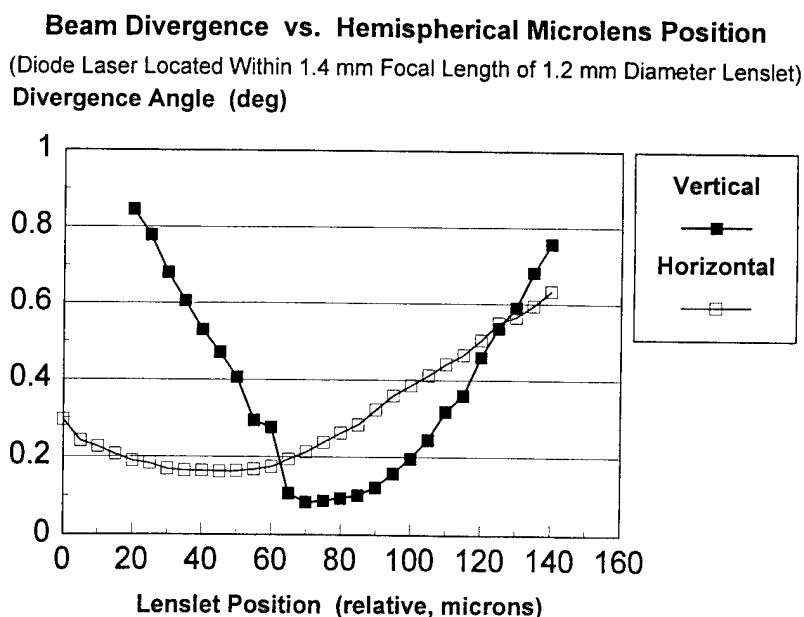


**Figure 37.** Transmitted diode laser beam divergence in two planes as a function of plano/convex microlens axial position within back focal plane of lenslet.

### 5.3 ASTIGMATISM CORRECTION

Our visible-red, edge-emitting diode laser designated as a source for collimation efficacy testing of printed microlenses was first measured for astigmatism using a microscope objective to amplify the beam and a beam analyzer system to find the minimum spot sizes in directions perpendicular and parallel (“fast” and “slow” diverging, respectively) to the laser bar. The raw data is shown in **Figure 38**, along with the astigmatism (difference in focal lengths) value,  $5.2 \mu\text{m}$ , calculated from the measured system amplification.

Since only a relatively slight degree of ellipticity is required in a lenslet to correct an astigmatism

on the order of only 5  $\mu\text{m}$ , the MRX-115

UV-resin material was used to print several series of lenslets with very gradually incremented

hemi-elliptical focal length and axes ratios, such as pictured in **Figure 39**.

These series of microlenses were made with diameters on the order of 1 mm to facilitate testing with our laser, by

depositing a total of 333 each 50  $\mu\text{m}$  diameter droplets on each of three print sites and varying the center-to-center site distances in increments of 20  $\mu\text{m}$ .

The dimensional uniformity of these microlenses was increased by printing them onto cover glass slides which had been treated for low

wetting with silanization solutions. The variation of the substrate plane dimensions and focal lengths for the lenslets of **Figure 39** are plotted in **Figure 40** as functions of deposition site spacings. Here, the lenslets made with print site spacings in the range

160-200  $\mu\text{m}$  are so nearly hemispherical that they have only one distinguishable focal point, within the sensitivity of the microscope imaging measurement method. As the spacings between these three sites are increased, the ellipticity becomes increasingly distinguishable, and the "slow"-to-"fast" focal and length-to-width ratios rise from 1.0 to maximum values of 1.26 and 1.19, respectively. The series of circular to slightly elliptical printed microlenses were used to predict empirically values for these ratios needed for correcting the astigmatism of our diode laser source.

Each of nine hemi-elliptical microlenses with incrementally differing axis ratios (pictured in

## DIODE LASER ASTIGMATISM DATA

Spot Widths in Parallel & Perpendicular (to bar) Directions  
Spot Width (at 75% max) (microns)

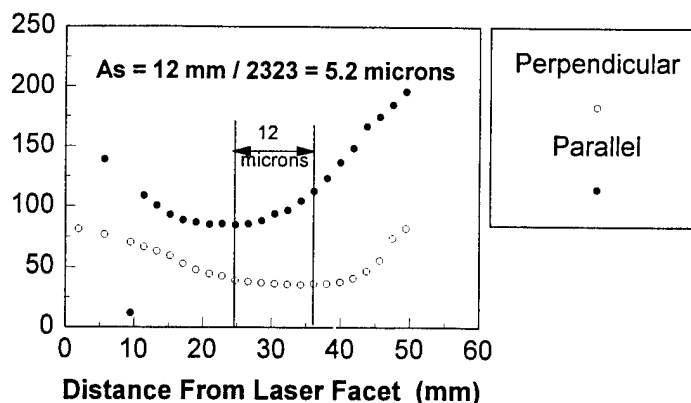


**Figure 38.** Amplified spot widths versus beam profiler moving distance along optical axis, from which astigmatism for this for this diode laser is calculated using optical system amplification factor.



**Figure 39.** Series of UV-cured microlenses, each printed by depositing droplets at three sites and increasing the distance between sites (L-to-R) by 20  $\mu\text{m}$  per lenslet, resulting in a gradual increase in ellipticity (Length/Width).

Figure 39) were positioned (as in Figure 36-B) between the diode laser source and a screen. Two sets of data were obtained for each microlens with major axis oriented alternatively perpendicular and parallel to the fast diverging irradiation plane of the laser. In each series the distance along the propagation direction which the lenslet had to be moved to bring alternatively the fast and slow diverging planes of radiation to a minimum dimension on the screen was measured.

The two sets of data for the 9 microlenses are plotted in Figure 41, where there are two data points for each lenslet, designated by its dimensional axis ratio calculated for the two orientations relative to the rapidly diverging "fast" axis of the diode laser. From the point of crossing of the best fit curve of the 0-line of the

**Dimensional & Focal Parameters vs. Site Spacing**  
(MRX115 on C1-Glass, 3 Sites, 333 ea 50 micron Droplets per Site)  
**Dimensions (microns)**

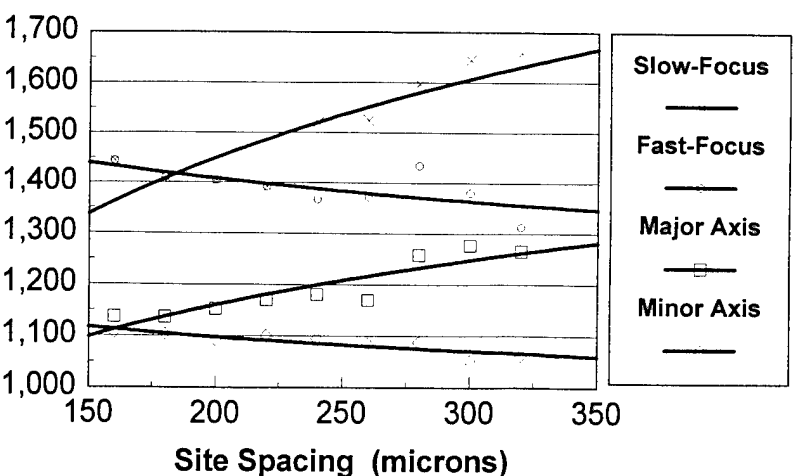


**Figure 40.** Variation of focal lengths and substrate plane dimensions with site spacings for UV-cured microlenses printed with 3 each depositions of 333 each droplets per lenslet.

**Laser Astigmatism Correction with Hemi-Elliptical Microlenses**  
(Axial Movements Required for 9 each Microlenses in Two Orientations)  
**Axial Movement (microns)**

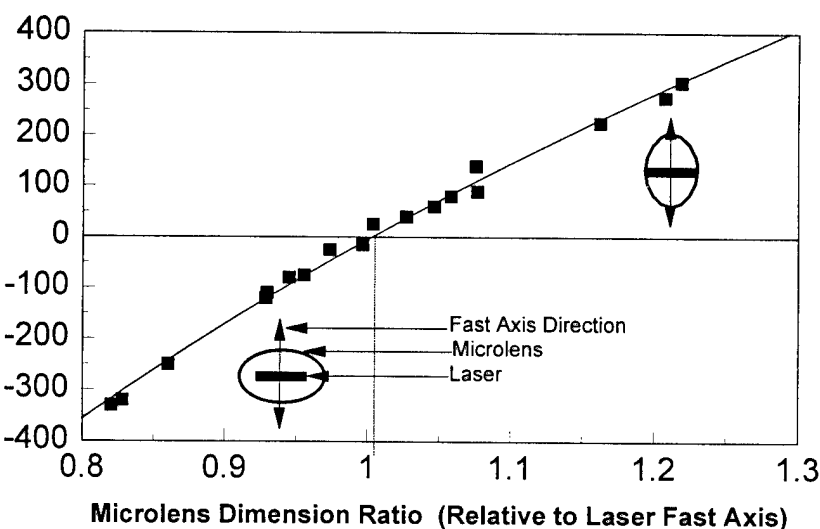


**Figure 41.** Axial movements required for each of 9 hemi-elliptical microlenses of Fig.1 to move between "fast" and "slow" focal planes of diode laser, for two depicted lenslet orientations relative to laser "fast" (most rapidly diverging) direction.

Y-axis, a dimensional axis ratio of a lenslet of this type which would correct exactly the laser's astigmatism can be deduced. In this case the ideal indicated dimension ratio is very close to 1 (about 1.001). From these experiments it may be concluded that such measurements could enable rapid optimization of printed microlens configurations for different diode laser sources.

Close inspection of these data indicate that the microlens closest to the  $Y=0$  line, the one having axis ratio the closest to unity, actually showed an over-correction (lenslet position for fast focus further from source than for slow focus). This effect was found to be related to slight imperfections in the shape symmetry of the printed lenslet, i.e., a slight off-axis sag in the lenslet of only a couple of microns, which become detectable in printed microlenses greater than  $\sim 500\text{ }\mu\text{m}$  in diameter. Subsequent investigation revealed that this sag was correlated with a slight gravitational effect due to the horizontal printing geometry (versus the vertical one shown in **Figure 4**) utilized at the time these data were obtained.

Reconfiguring the printing direction from horizontal to vertical greatly improved the symmetry of printed microlenses. For example the imaging qualities of 1 mm diameter hemispherical lenslets printed in the vertical- & horizontal-microjetting configurations are compared in **Figure 42**. Here each microlens was positioned in front of a visible diode laser, with substrate back surface facing the laser, and the transmitted image was recorded with our rotating knife-

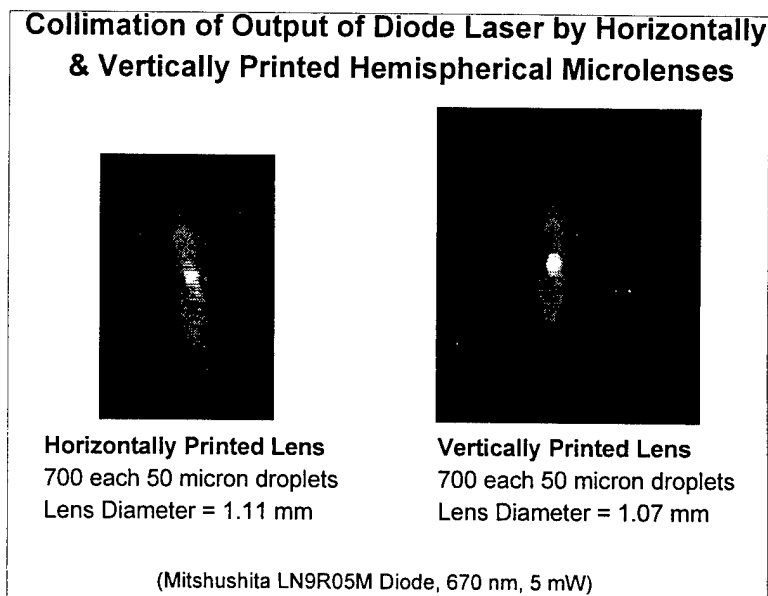


**Figure 42.** Images of diode laser beam waist transmitted by differently printed 1 mm hemispherical microlenses, showing significantly less distortion for the vertically printed one on the right.

edge, silicon-detector-based BeamAnalyzer<sup>®</sup> system. Both images show spreading of the intensity distribution in the vertical, high-output-divergence direction due to spherical aberrations.

However, the image transmitted by the vertically printed lenslet shows significantly less distortion in the measurement plane and, unlike that from the horizontally printed one, does not rotate as the lenslet is moved along the optical axis relative to the laser. Clearly, verticalization of the Micro-optics Printing Station appears to have eliminated the shape anisotropies previously affecting optical performance in vertically printed microlenses.



## 6.0 PRINTED MICROLENS CHARACTERIZATION

### 6.1 PLACEMENT, DIMENSIONS AND FOCAL LENGTH

The *accuracy of placement* of printed microlenses is determined by the following factors:

- (a) resolution and absolute accuracy of the XY stages for positioning the target substrate;
- (b) directional constancy of the print head microjetting trajectory;

The positioning stage systems employed on the Micro-optics Printing Station have stepping resolutions and straight line accuracies of 0.5  $\mu\text{m}$  and 2  $\mu\text{m}/\text{inch}$  travel, respectively.

Consequently, most of the error in microlens placement comes from angular deviations of the microjet trajectory over time.

An experiment was performed to measure the inherent stability of the microjet trajectory over time. A microjet device was first set up (in a horizontal orientation) with an LED strobe and microscope perpendicular to the device, to enable viewing of the superimposed images of ejected droplets (like the photo of Fig. 3 ). A video caliper was used to measure at periodic intervals the positional movement of ejected microdroplets of test fluid perpendicular to the initial trajectory. The geometry is shown at the top of **Figure 43**, which gives series of positional data for the droplet image perpendicular to the device axis, measured over two different time periods, at intervals of 1 min. Here the resolution of the measurement of droplet position was  $\pm 1.2 \mu\text{m}$ . It can be seen that the maximum deviation of trajectory was about 2  $\mu\text{m}$  at a distance of 2-3 mm from the device orifice. Since printing is done at orifice-substrate distances in the range 0.5-1 mm, it may be concluded that the microjet device is *inherently* capable of printing consistently to a designated target location to within  $\pm 1 \mu\text{m}$ . Of course, random events such as the appearance of a particle at the orifice which is too large to be ejected can cause intermittent and large deviations in droplet trajectory. This rarely happens in practice because of the presence of a 10  $\mu\text{m}$  in-line filter upstream of the microjetting device.

To determine the *actual* microdroplet placement repeatability when printing with an optical material and performing relatively large stage excursions, the following experiment was performed. The print head was shuttled over a 4 cm distance between a “home” and the “print” position ten times, each time

depositing a single 60  $\mu\text{m}$  droplet at the same nominal “print” location on the substrate. The results, shown in the micrograph of **Figure 44**, provide an example of the level of placement accuracy achieved with the stage systems in printing optical materials. The maximum placement error seen here, due undoubtedly to variations in droplet trajectory rather than encoder error, would appear to be less than about 5  $\mu\text{m}$ , representing a straight line placement error of about 3  $\mu\text{m}$  per inch of travel.

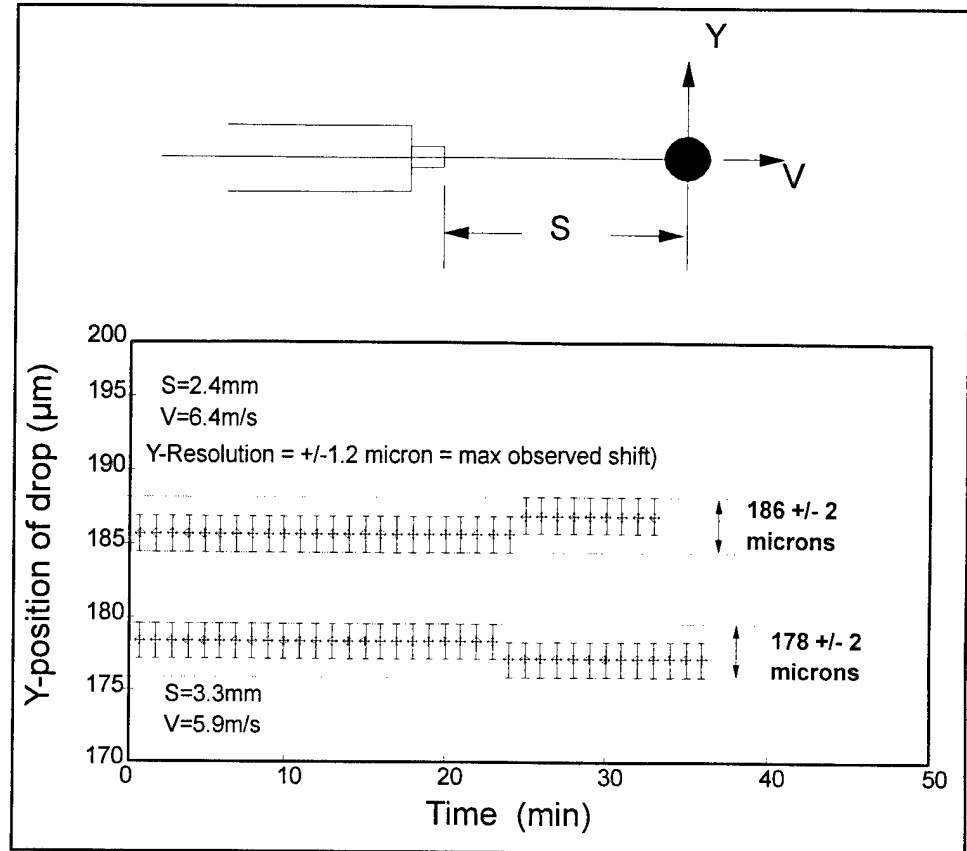


**Figure 43.** Data demonstrating the 2 $\mu\text{m}$  spatial stability over extended periods of time of 50 $\mu\text{m}$  droplets, microjetted at 5,000 Hz and stroboscopically “frozen” in space and time.

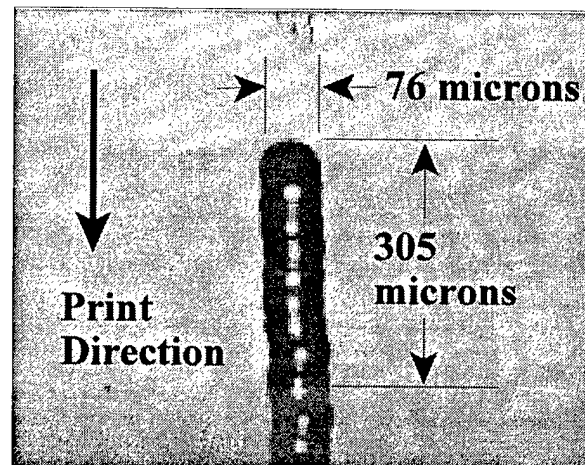


**Figure 44.** 10 each repeated 4 cm Shuttle-stage translations & printings at 150  $^{\circ}\text{C}$  of a 60  $\mu\text{m}$  droplet of optical thermoplastic.

To test the *dimensional* reproducibility of hemispherical microlenses printed onto horizontal substrates, a 10X10 array of 500  $\mu\text{m}$  diameter (nominal) lenslets was printed onto low-wetting glass with the MRX-115 material. A RAM-Optical vision system was then used to measure the average diameter (using 1000 point sampling) of each lenslet, utilizing its automatic edge detection capability. A statistical analysis of the data is shown in **Figure 45**, where the distribution appears to be fairly uniform, and the standard deviation from the average diameter value is on the order of 1%.

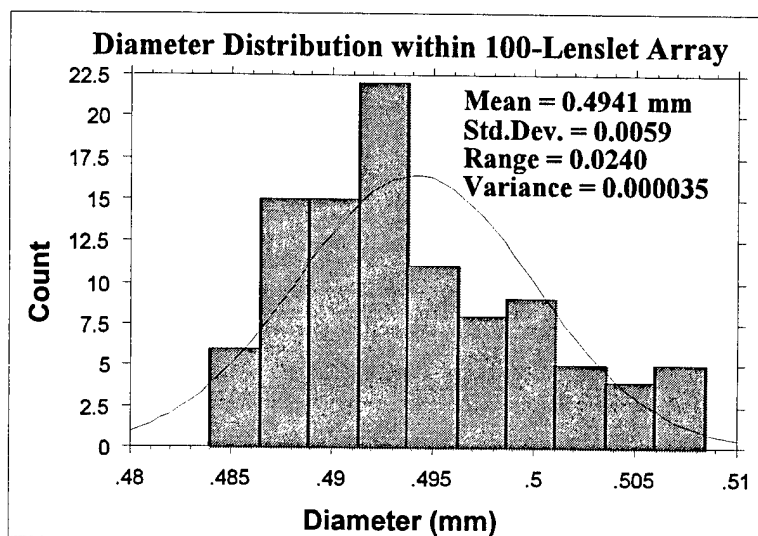


**Figure 45.** Distribution of diameters of vertically printed hemispherical microlens of MRX-115 material within a 100 lenslet array, showing standard deviation of 1.2% (5.9  $\mu\text{m}$ ) from average diameter of 494  $\mu\text{m}$ .

The *focal lengths* of these 100 microlenses were measured with a microscope at 600X, using a digital stage-height read-out and measuring the distance from the substrate to the imaging plane, at which the edges of the condenser lens aperture (at its smallest setting) come into clearest focus. A statistical analysis of the focal length data is given in **Figure 46**.

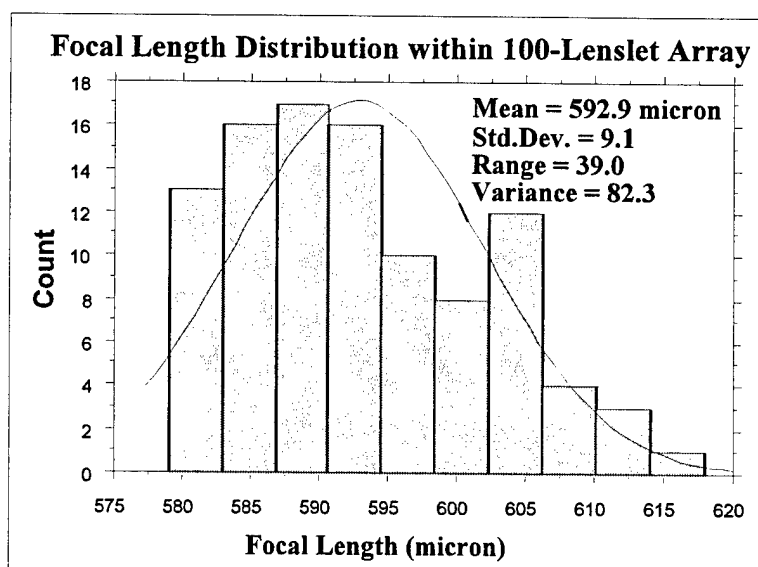


**Figure 46.** Distribution of focal lengths of the 100 vertically printed, 0.5  $\mu\text{m}$  diameter microlenses for which diameter data are given in Figure 45, showing standard deviation from the average value of 1.5%.

Again the distribution is seen to be relatively uniform and the standard deviation from the average focal length to be 1.5%.

Average diameters and focal lengths for nine arrays with differently sized hemispherical microlenses printed with UV-curing resin onto low-wetting glass are shown as further examples in **Table 1**. Here the number of 65  $\mu\text{m}$  droplets per site was varied between 1 and 500, and the data for each were obtained by measuring four, randomly chosen, lenslets from each array. The standard deviations from the average values of diameter and focal length for each array are seen to be mostly within  $\pm 1\%$  over a microlens diameter range 82-744  $\mu\text{m}$ .

**Table 1.** *Variation in average & standard deviations of hemispherical microlens diameters and focal lengths with number of deposited droplets of MRX-102uv-curing resin.*

Number of Droplets	Diameter Average ( $\mu\text{m}$ )	Diameter Std. Dev. (%)	Focal Length Average ( $\mu\text{m}$ )	Focal Length Std. Dev. (%)
1	81.7	0.76	99.8	1.26
2	103.8	0.48	133.0	0.62
5	142.3	0.67	246.8	0.82
10	178.0	0.79	283.8	1.64
20	229.8	2.10	347.8	0.43
50	310.3	1.47	457.5	1.09
100	397.3	0.72	591.3	1.56
200	511.3	0.58	779.5	1.43
500	744.0	0.57	1124	0.07
Average Standard Deviations		0.90		0.99

## 6.2 SURFACE CONTOUR UNIFORMITY

As a method for detecting irregularities or flaws in printed microlens *contours* an interferometric measuring system was set up as illustrated in **Figure 47**. Here we have a coherent laser source focused to a spot size which is small

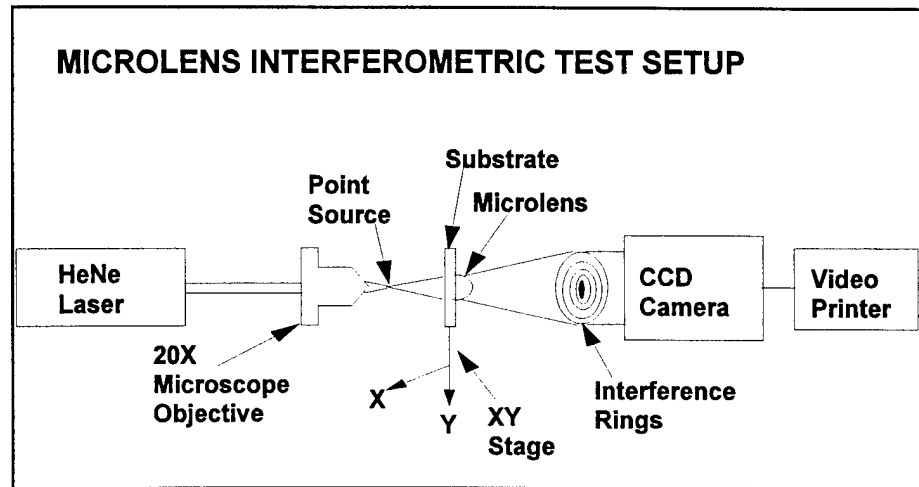


**Figure 47.** *Experimental setup for obtaining interference ring patterns from individual microlens for qualitative comparisons of uniformity of shape and surface smoothness.*

relative to the lenslet under test. This point source of light diffracts through the lenslet which changes the spherical curvature of the wavefront, and adds an aberration function onto that portion of the source wavefront passing around but not through the lenslet. The constructive and destructive interference between the two phase front components forms a visible ring pattern which is recorded via a camera and printer. An example interference pattern obtained for a well formed hemispherical microlens is shown in **Figure 48**. The *symmetry* and *uniformity* of these patterns reflect the actual symmetry and degree of surface regularity of the test microlens surface, but the fringes obtained in this way may not be used to determine quantitatively the lenslet contour (as the

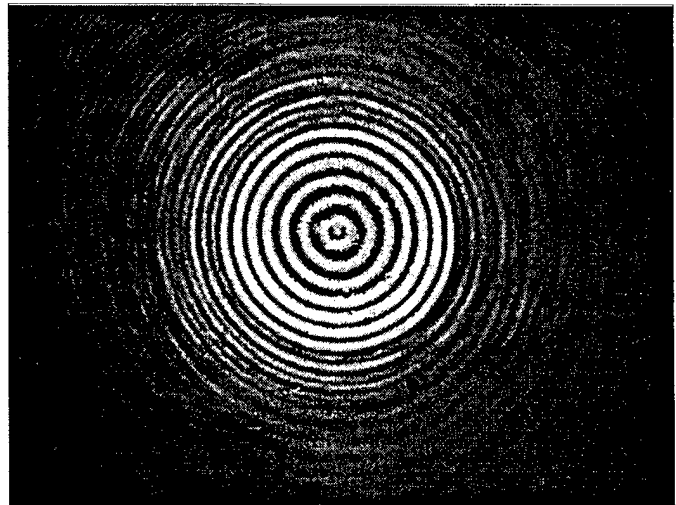


**Figure 48.** *Interferometric pattern of 120 μm diameter hemi-spherical microlens printed with optical thermoplastic at 215 °C.*

microlens height is typically two orders of magnitude greater than the wavelength of light being used). Once the set-up is optimized and aligned, the testing of many microlenses is simple and fast. One can readily separate damaged or poorly formed from undamaged or well formed lenslets by visual inspection of the recorded CCD. Here the rings are highly circular and uniform, indicating excellent shape symmetry and no significant surface irregularities. In contrast, the interference pattern for another similarly sized

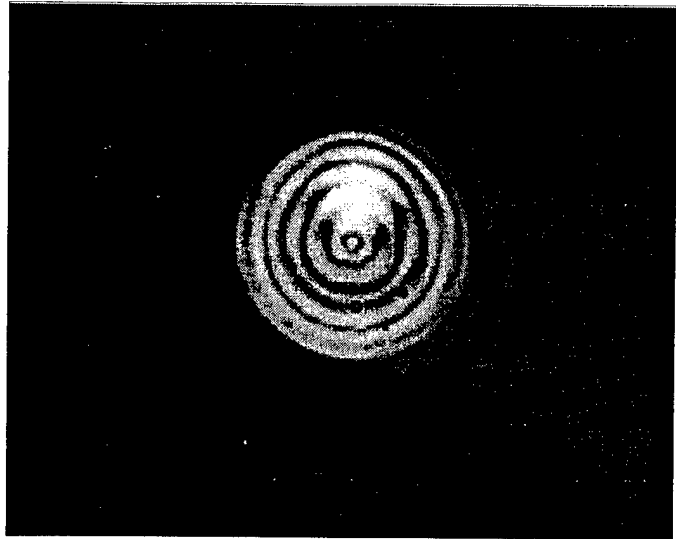


**Figure 49.** *Interferometric pattern from a slightly damaged and mis-shaped hemispherical microlens.*

hemispherical microlens shown in **Figure 49**, reveals an area of non-uniformity just above its center. This defect appears to be an indentation caused by contact damage incurred after printing. Similar interference patterns from "good" *hemi-elliptical* and *square-shaped* lenslets are given in **Figures 50 & 51**, respectively. Close inspection of these photographs reveals that the ring patterns have the two-fold and four-fold, versus circular, symmetries of the lenslets under test.

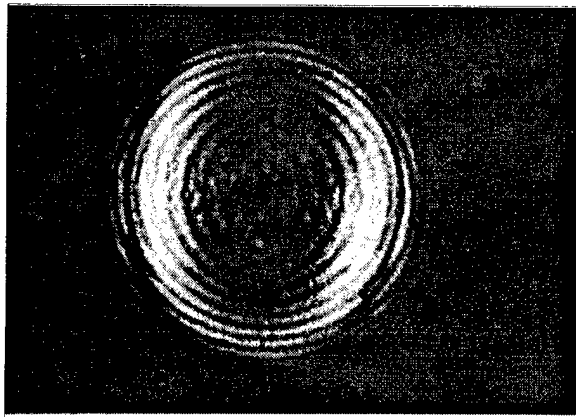


**Figure 51.** *Interferometric pattern of 304  $\mu\text{m}$  X 196  $\mu\text{m}$  hemi-elliptical microlens printed with optical thermoplastic.*

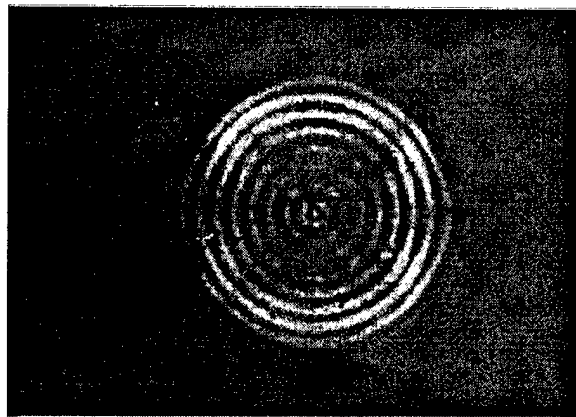


**Figure 50.** *Interferometric pattern of 212  $\mu\text{m}$  wide square shaped microlens printed by deposition of 3X3 pattern of 50  $\mu\text{m}$  droplets of optical thermoplastic.*

It is clear from these photographs that such data, at the very least, reflect the symmetry of the lenslet under test and are useful in detecting shape anomalies such as "dimples" or "dents" which may not be obvious from direct inspection with an optical microscope. By obtaining a better understanding of the detailed diffraction theory leading to these patterns, we should also be able to extract useful, quantitative information about lenslet aberrations from the data.

### 6.3 POWER POINT SPREAD DISTRIBUTION

A key measure of lenslet quality is the degree to which it exhibits "diffraction-limited" performance in the focusing of collimated light. This can be measured by performing a scan across its focal spot to determine its FWHM (full width at half maximum) value, then calculating the ratio of measured to theoretical FWHM. This ratio provides a quantitative, Figure-of-Merit (FOM) value (ideally, FOM=1.0) for the degree to which a lenslet is diffraction limited, i.e., is free of spherical aberrations. The theoretical FWHM may be calculated from diffraction theory using the focal length and diameter of the microlens under test, and may be shown to be proportional to wavelength and lenslet speed

$$[\text{FWHM}(\text{theory}) = 1.029 * \lambda * (f/\#)].$$

To determine the optical quality of printed UV-curing hemispherical microlenses, a beam analyzer system with rotating knife edges was utilized, in conjunction with a HeNe laser source and a relay lens. The system provides data in the form of scans along one or two directions perpendicular

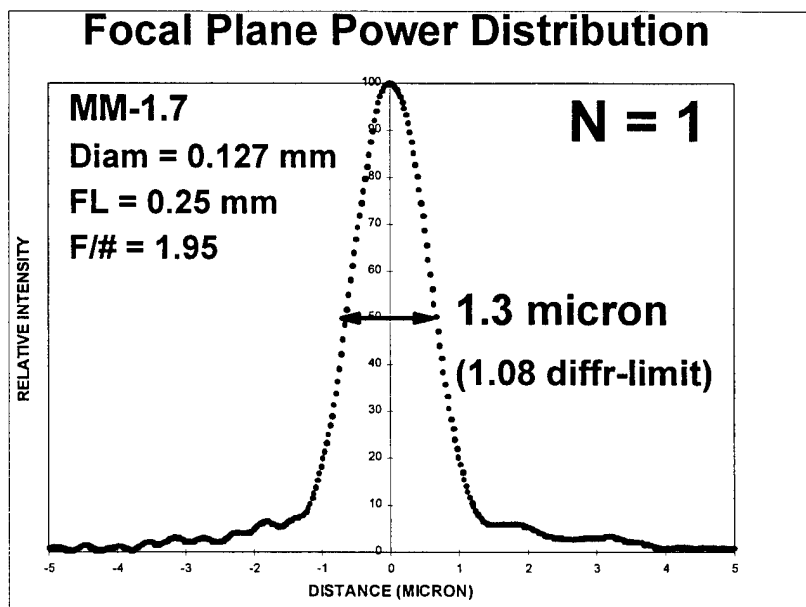


**Figure 52.** Relative intensity versus scan distance for 127  $\mu\text{m}$  diameter, 1.08 diffraction-limited lenslet printed with one 50  $\mu\text{m}$  droplets of UV-curing material.

to the propagation axis and 3D-simulations of the power distribution of the focal peak.

A focal plane power point spread distribution peak for a typical hemispherical microlens printed with a single ( $N=1$ ) 50  $\mu\text{m}$  droplet of UV-curing resin is given in **Figure 52**. Here it can be seen that the FWHM value of 1.3  $\mu\text{m}$  for the focal spot of a 127  $\mu\text{m}$  diameter lenslet with 250  $\mu\text{m}$  focal length is, by this measure, nearly diffraction limited ( $\text{FOM}=1.08$ ). In addition the distribution of power in the focal plane is quite uniform, as seen in the two dimensional and simulated-three dimensional scans of **Figures 53 & 54**, respectively.

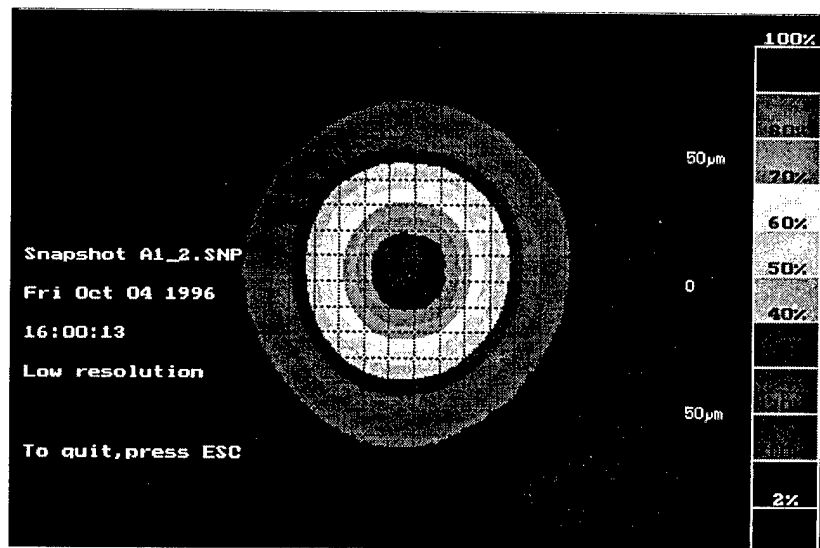


**Figure 53.** 2D power distribution of focal spot for 1-drop lenslet of Fig. 52.

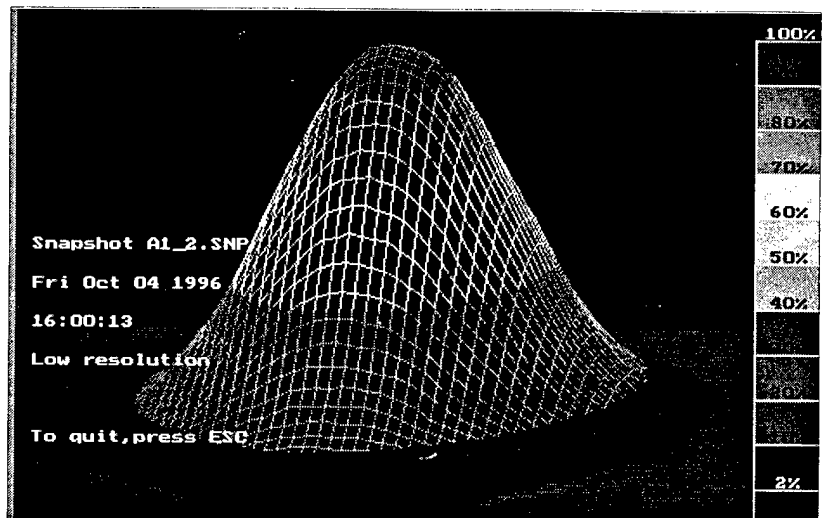


**Figure 54.** 3D focal plane power distribution of  $N=1$  lenslet of Fig. 52.

As the diameter of such lenslets is increased by depositing additional droplets of material the relative distribution of focal plane power remains virtually unchanged. This is illustrated by the nearly identical width and diffraction limited performance of peak for a microlens of the same material printed with a 10X increase in volume, shown in **Figure 55**. Data obtained for similarly sized hemispherical microlenses printed with optical thermoplastic material are quite similar to



those printed by deposition of UV-curing optical resin.

It would seem that this capability for printing nearly diffraction limited hemispherical microlenses with highly durable optical material (UV-curing resins) over a wide range of lenslet diameters is a key selling point for this micro-optics printing technology.

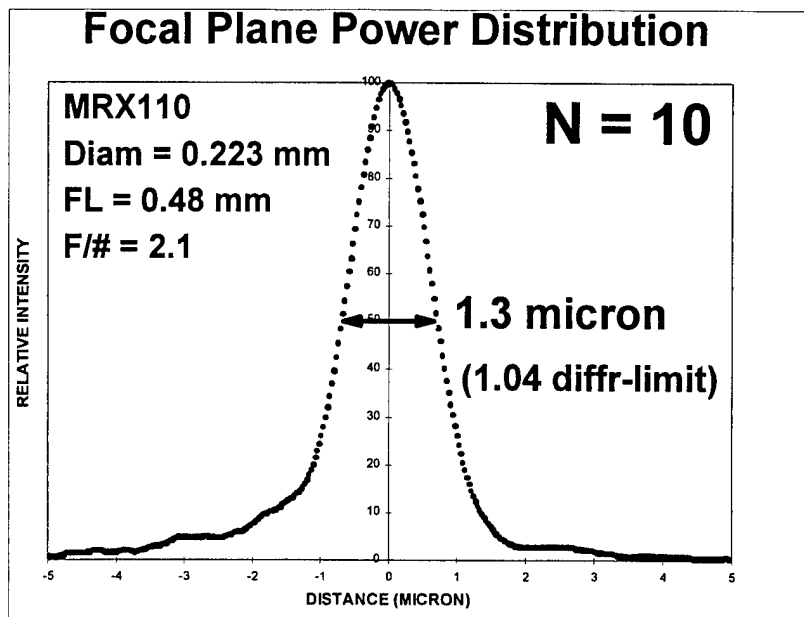


**Figure 55.** Focal peak for 223  $\mu\text{m}$  diameter, 1.04 diffraction-limited lenslet printed with ten 50  $\mu\text{m}$  droplets of UV-curing material.

Power distribution peaks obtained for hemi-elliptical microlenses printed with optical thermoplastic also indicate tight focusing (narrow peaks) in the "fast" and

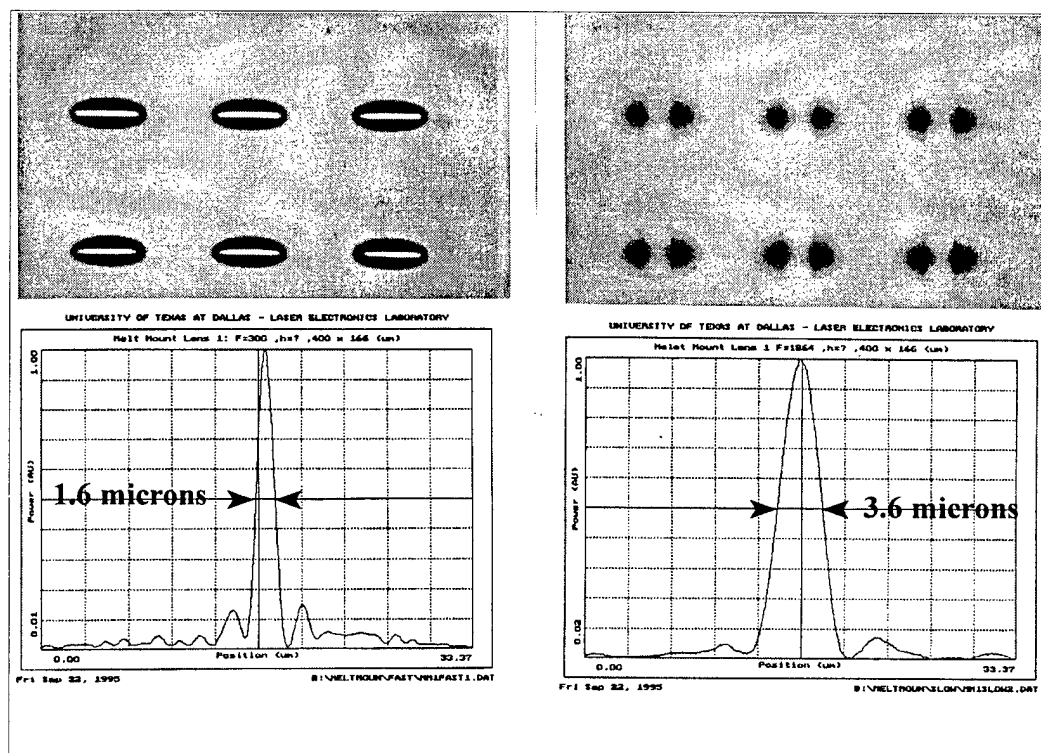


**Figure 56.** Power scans across "fast" (left) & "slow" (right) focal lines of a printed hemi-elliptical microlens lens from the array shown above in "fast" & "slow" focus planes, at 300  $\mu\text{m}$  & 1,864  $\mu\text{m}$  from substrate plane.

"slow" focal planes. An example is shown in **Figure 56**, where the power distribution peaks were obtained by scanning a pin hole across the focal lines and imaging onto a CCD camera.

#### 6.4 MODULATION TRANSFER FUNCTION

The Modulation Transfer Function (MTF), of a lens (i.e., the ratio of image-to-object modulation for sinusoids of varying spatial frequency,<sup>24</sup> or the magnitude of the Fourier transform of a point source image<sup>25</sup>) is a more sensitive indicator of the imaging performance of a lens than the FWHM of its power point distribution peak discussed above. To obtain imaging performance data using the MTF figure of merit, an extensive series of measurements of the Modulation Transfer Function (MTF) of three differently sized hemispherical microlenses printed vertically with MRX-115 optical resin was performed, and the data were compared to a commercial macrolens.<sup>26</sup>

The setup used to perform the MTF measurements is illustrated in **Figure 57**. Here narrowband light (665 nm) from a high luminance red LED is passed through a diffuser and a pinhole filter to create a nearly point source of diverging light to fully illuminate the surface of the microlens under test, at a pin-hole-to-lens

separation of 3 cm (where the light distribution across the microlens can be approximated as a plane wave). The focused light from the microlens is then collected by a 100X magnification microscope objective to expand the otherwise under-sampled beam cross section onto a color CCD camera, 9 cm distant from the objective lens. The image of the source at focus, i.e., the Point Spread Function

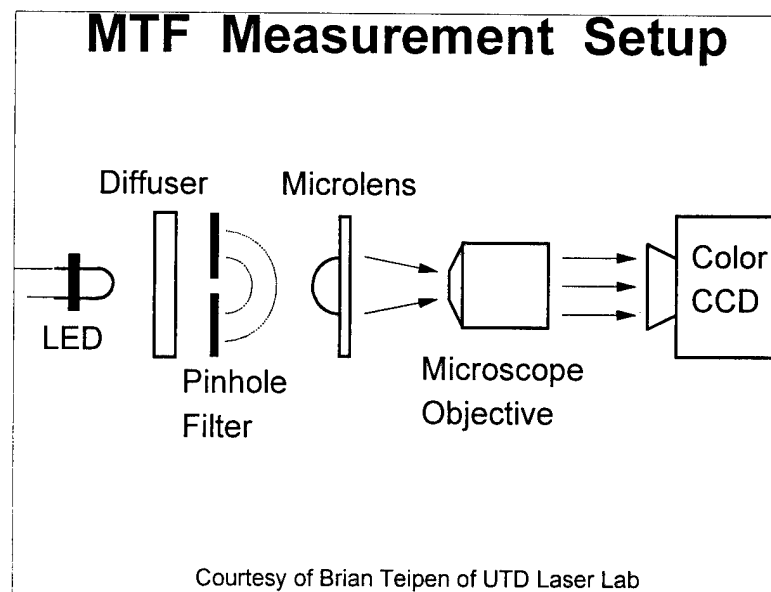


**Figure 57.** *Experimental configuration for measuring Modulation Transfer Function of a microlens (Ref.27).*

(PSF), is captured by a frame grabber for subsequent analysis. The 3D PSF for a 1-drop printed hemispherical microlens having diameter and focal length of 109  $\mu\text{m}$  and 136  $\mu\text{m}$ , respectively, as given in **Figure 58**, is an initial indicator of good optical performance. The Line Spread Function (LSF) for this lenslet, obtained by integrating across an axis of the intensity matrix, is given in **Figure 59**. Here the sharpness of the peak, having a full width at half maximum distance of only 1  $\mu\text{m}$ , is a more quantitative indicator of the low spherical aberrations of this lenslet.

Fourier transforming the PSF of **Figure 58** yields a 3D MTF for the 1-drop printed microlens. A typical cross-section through this Modulation Transfer Function is given in **Figure 60**, along with the theoretical diffraction-limited

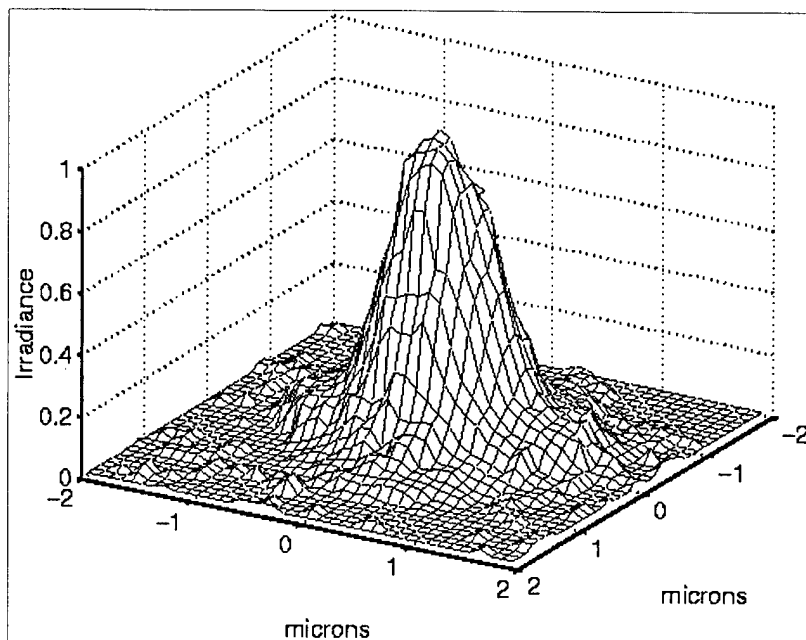


**Figure 58.** Point Spread Function (PSF) for a microlens printed with one 50  $\mu\text{m}$  droplet of MRX-115 optical resin, shown as irradiance versus distances in microns in the focal plane (Ref.27).

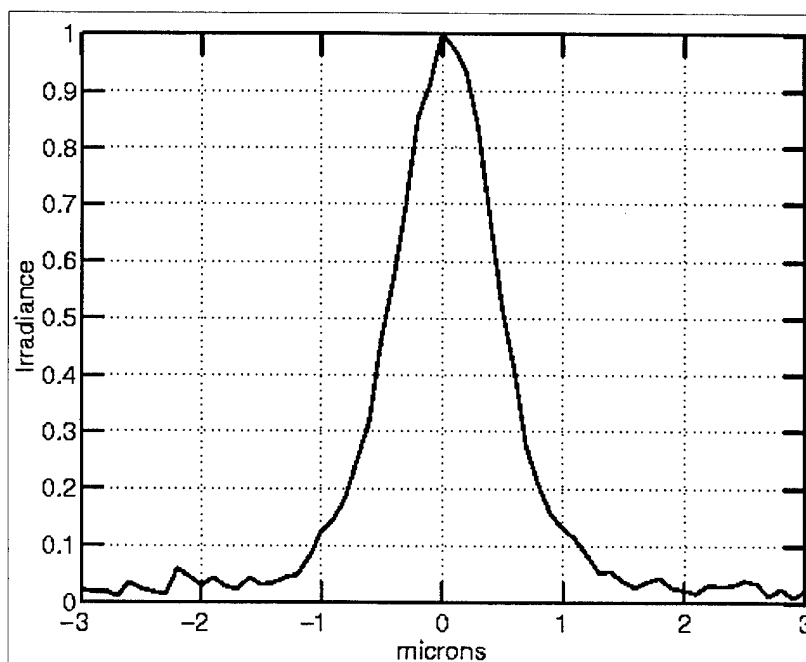


**Figure 59.** Line Spread Function (LSF) calculated from Fig. 2 for the printed 1-drop microlens, shown as irradiance versus distance in microns, where FWHM is 1  $\mu\text{m}$  (Ref.27).

MTF for an ideal lens with identical  $f/\#$  of 1.25. For this wavelength of light and  $f/\#$  the theoretical cutoff frequency is approximately 1200 lp/mm. The Strehl Ratio, obtained from the ratio of integrated areas under the measured and theoretical curves, is 0.71 for this 1-drop microlens, indicating relatively little spherical aberration for this measurement configuration.

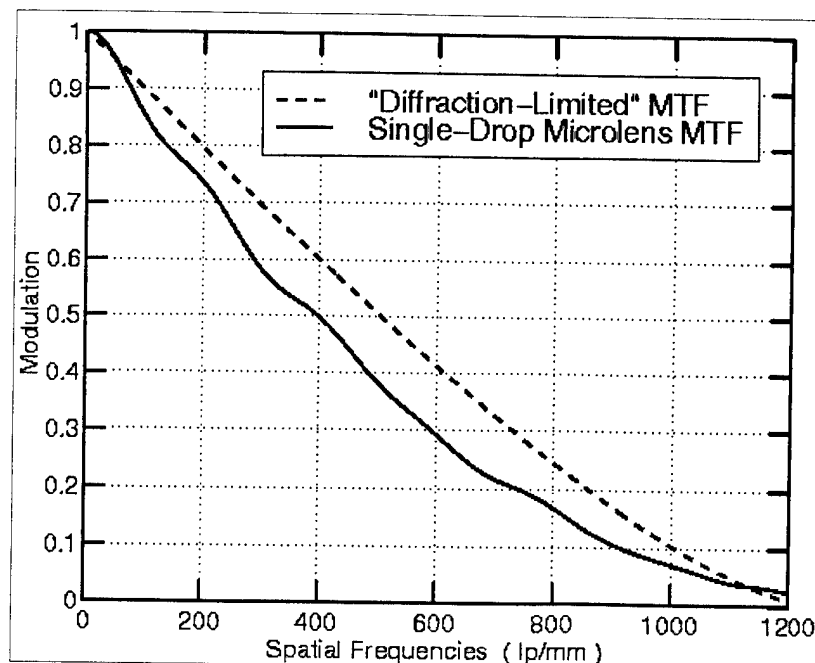


**Figure 60.** Typical Modulation Transfer Function of a 1-drop microlens printed with MRX-115 UV-curing resin, compared to theoretical result for same  $f/\#$  (1.25) (Ref.27).

As the diameters of lenslet under test increase, there is a corresponding drop in this figure of merit. For example, Strehl Ratios obtained in the same way for a printed 3-drop microlens (diameter & focal length 117  $\mu\text{m}$  & 143  $\mu\text{m}$ , respectively) and an off-the-shelf macrolens (diameter & focal length of 52 mm & 100 mm, respectively) were 0.58 and 0.13, respectively.

It was concluded from these measurements that for similar  $f/\#$ 's the smaller microlenses outperform the macrolens by having significantly greater Strehl Ratios, i.e., are closer to the diffraction-limited case, at similar cutoff modulation frequencies. The data obtained with this series of experiments confirmed those from the other types of measurements discussed above, in that these printed microlenses are of sufficient optical quality to be utilized in imaging applications.

## 7.0 PRINTED MICROLENS DESIGN & MODELING

### 7.1 HEMISPHERICAL MICROLENSSES

In the design of printed hemispherical microlenses to meet a specific set of performance specifications, it is convenient to model them as caps cut from spheres of the appropriate radius, which are the radii of curvature of the plano/convex normal to the substrate, as illustrated in **Figure 61**. For a certain material with an index of refraction of  $n$ , the focal length of the plano-convex lens depends only on the radius of curvature  $R$  of the lens surface [ $f = R/(n-1)$ ]. However,  $R$  can not be measured directly and has to be replaced by other measurable parameters.

The readily measurable dimensions for a printed hemispherical microlens are diameter ( $d=2a$ ) and height ( $h$ ), and the volume ( $V$ ) is precisely determined by the size and number of droplets used to print it.

From **Figure 61** the diameter  $d$ , height  $h$  and volume  $V_l$  of a printed microlens are related to the radius of the corresponding sphere as

$$d = 2\sqrt{2Rh - h^2} \quad , \quad (1)$$

$$V_l = \frac{\pi}{3} h^2 (3R - h) \quad (2)$$

The volume  $V_d$  of a dispensed droplet of diameter  $d_d$  is

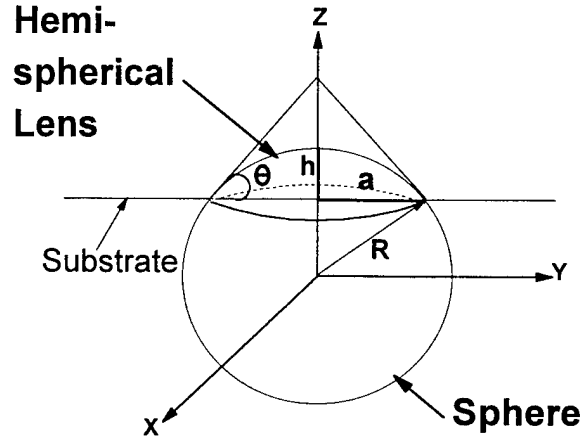


**Figure 61.** Model of printed hemispherical microlens as cap cut from a sphere of radius  $R$ , where  $a$ ,  $h$  &  $\theta$  are microlens substrate-plane-radius, height & substrate contact angle, respectively.

$$V_d = \frac{1}{6} \pi d_d^3 . \quad (3)$$

The volume of a lenslet consisting of  $N$  droplets is then

$$V_l = N V_d , \quad (4)$$

so we have

$$N V_d = \frac{2}{3} \pi R^3 - \frac{\pi}{3} (2R^2 + \frac{d^2}{4}) \sqrt{R^2 - \frac{d^2}{4}} . \quad (5)$$

If  $f$  is predetermined (i.e.,  $R$  is predetermined) by the optical system requirements. 4-6 can be transferred to the forms of  $R = R(d, h)$ ,  $R = R(V_l, h)$  and  $R = R(V_l, d)$ . This means that any two parameters from  $(d, h, v_l)$  can fully determine  $R$ . Among them  $d$  is the easiest one to measure and has the accuracy of  $\pm 1\%$ . As to  $h$ , its measurement accuracy is currently about  $\pm 5\%$ . Eq. 5 can not be solved simply, but we have used spread sheet programs to obtain numerical results.

We have also used this simple model of a hemispherical microlens as a cap-section of a sphere of the appropriate radius to calculate a theoretical height for a lenslet from its measured diameter and substrate contact angle, e.g., the angle between the substrate surface and the tangent to the lenslet profile at the surface, as illustrated above in **Figure 61**. The substrate contact angles for printed hemispherical microlenses greater than about 400  $\mu\text{m}$  in diameter were measured with a contact angle measuring goniometer at 10X magnification. Here a calculated lenslet height may be determined from its measured diameter  $d$  and contact angle  $\theta$  as

$$h = \frac{d (1 - \cos\theta)}{2 \sin\theta} , \quad (6)$$

Data for the calculated and measured heights, as well as the NA values for a series of UV-resin microlenses in the 700-1,200  $\mu\text{m}$  range printed onto low wetting glass are shown in **Figure 62**.

Comparison of the lenslet height curves shows exact agreement between measured and calculated values occurs at a lenslet diameter of 1,050  $\mu\text{m}$ , with the actual values being less and greater than the calculated ones below and above that diameter,

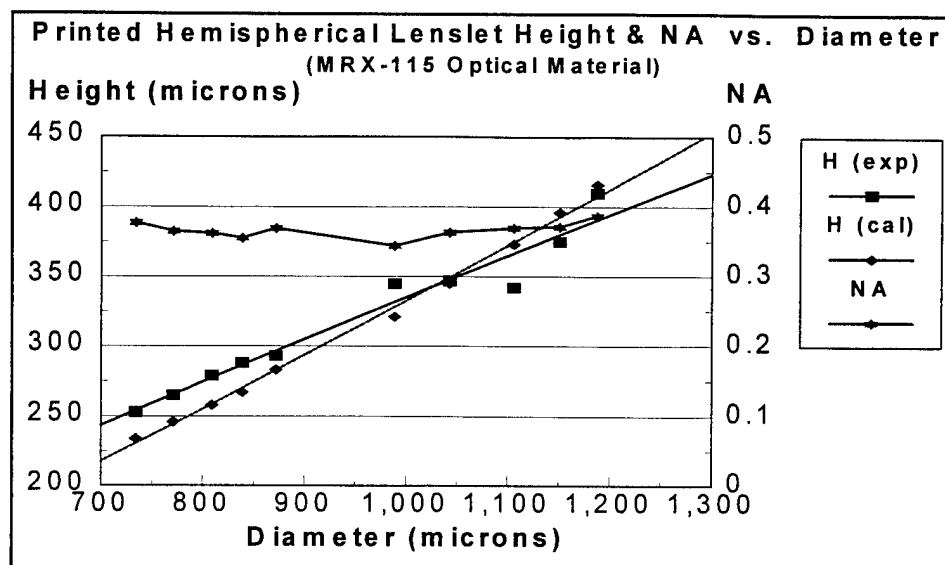


**Figure 62.** Comparison of measured and calculated (from diameter and contact angle) heights and calculated (from diameter and focal length) numerical apertures for a range of printed hemispherical microlenses.

respectively. However, the numerical aperture of the lenslets remains relatively constant at about 0.37.

## 7.2 HEMI-ELLIPTICAL MICROLENSES

A model for predicting the geometry of ellipsoidal microlenses fabricated by the photoresist melting method has been recently presented.<sup>27</sup> Here we develop some analytical equations for calculating the focal lengths of printed hemi-elliptical microlenses from their geometries, using certain approximations. This type of model may be useful, for example, in estimating the hemi-elliptical microlens geometry required to achieve the focal lengths needed for a specific application.

Some analytic equations governing the optical properties of the hemi-elliptical anamorphic

microlenses may be derived if we assume an ellipsoidal geometry. From these equations we may then calculate the “fast” and “slow” focal lengths of a printed lenslet from dimensional and volumetric measurements and compare them with measured focal length data.

As shown in **Figure 63**, such a lenslet may be modeled as the top slice of a full ellipsoid described by:

$$\frac{x^2}{a^2} + \frac{y^2}{b^2} + \frac{z^2}{c^2} = 1 \quad (7)$$

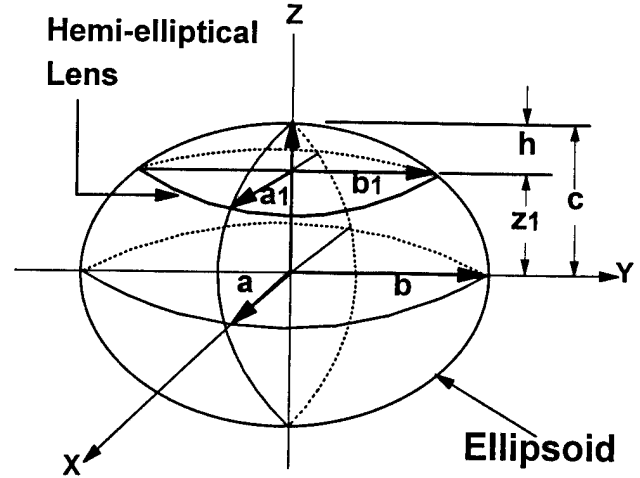


**Figure 63.** Hemi-elliptical lens cut from top of an ellipsoid with radii  $a, b, c$ , having major & minor substrate-plane axis radii of  $a_1$  &  $b_1$  and height  $h$ .

The length at the substrate surface of the major ( $2 \times b_1$ ) and minor ( $2 \times a_1$ ) axes of a printed hemi-elliptical microlens may be measured at 100-600X with an optical microscope. The height ( $h$ ) of such a lenslet may be measured in profile at the same magnifications using long working distance objective lenses. The volume of a dispensed microdroplet of optical material used to print the lenslet remains quite constant and may be measured accurately. The volume of the printed microlens ( $V_1$ ) is then known from the number of droplets used to print it. The parameters of the corresponding ellipsoid may then be expressed in terms of these four measured quantities of a printed hemi-elliptical microlens as:

$$c = \frac{h}{3} \frac{3V_1 - \pi a_1 b_1 h}{2V_1 - \pi a_1 b_1 h} \quad (8)$$

$$a = \frac{a_1 c}{\sqrt{2ch - h^2}} \quad (9)$$



$$b = \frac{b_1 c}{\sqrt{2ch - h^2}} \quad (10)$$

Approximate focal lengths of the lens may be found from the radii of curvature of the ellipsoid taken at the top of the lens. There is a radius of curvature in the X direction  $R_x$ , and one in the Y direction,  $R_y$ .  $R_x$  and  $R_y$  may be found from the calculus in terms of first and second derivatives. In particular we use the radius of the osculating circle, which is the circle with the highest degree of contact with the ellipse.<sup>28,29</sup> Given the microlens material index of refraction,  $n$ , the “fast”( $f_x$ ) and “slow”( $f_y$ ) focal lengths of a printed hemi-elliptical microlens may be calculated (approximately) as:

$$f_x = \frac{R_x}{(n-1)} = \frac{a^2}{(n-1)c} = \frac{a_1(3V_1 - \pi a_1 b_1 h)}{(n-1)c\pi b_1 h^2} \quad (11)$$

$$f_y = \frac{R_y}{(n-1)} = \frac{b^2}{(n-1)c} = \frac{b_1(3V_1 - \pi a_1 b_1 h)}{(n-1)c\pi a_1 h^2} \quad (12)$$

We note in passing that from these equations the ratio of the two focal lengths may be expressed as the ratio of the squares of the corresponding radii of either the printed microlens or the full ellipsoid:

$$\frac{f_x}{f_y} = \frac{a^2}{b^2} = \frac{a_1^2}{b_1^2} \quad (13)$$

As a test of this model, a series of nine arrays of hemi-elliptical microlenses was fabricated. The lenslets were printed using six each 71  $\mu\text{m}$  diameter droplets of 1.704 index optical thermoplastic deposited on center-to-center spacings varying from 30  $\mu\text{m}$  to 70  $\mu\text{m}$ , then measured for length, width, height, and “fast” & “slow” focal lengths relative to the substrate plane. The dimensions of each lenslet were used in Equations (2)-(4) to calculate the radii of the corresponding ellipsoid, then Equations (5) & (6) were applied to obtain focal length values. These calculated focal lengths and the measured ones are plotted for comparison as a function of deposited droplet spacing in **Figure 64**. Here it is seen that there is a very good correspondence between calculated and measured values of the “fast” focal lengths. However, the calculated “slow” focal lengths tend to exceed the measured ones,

and this difference rises as the lengths of the microlenses increase with droplet spacing. This increasing deviation between measured data and modeled values is probably due both to the oscillating circle and paraxial approximations used in deriving the equations and to the inaccuracies involved in measurement of lenslet height in profile with an optical microscope (due to diffraction effects).

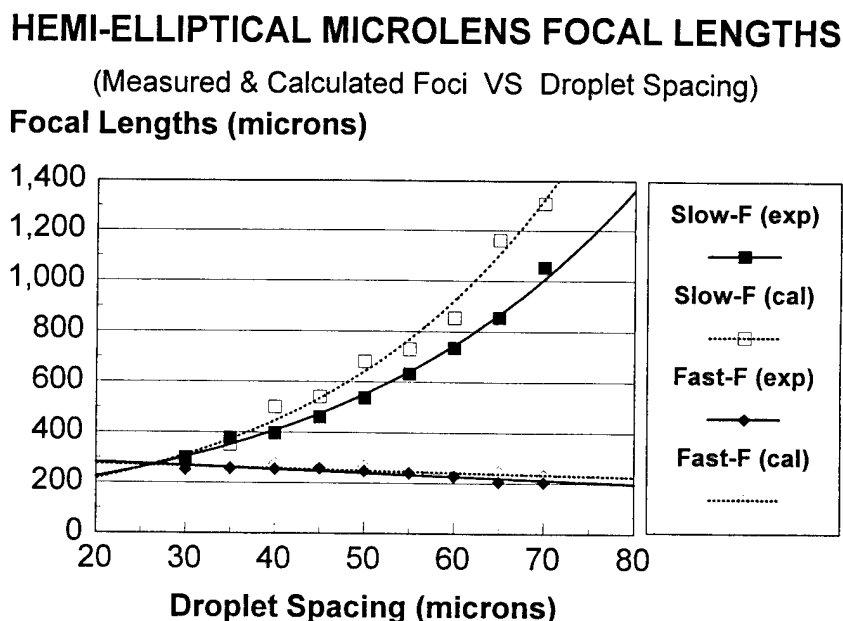


**Figure 64.** Comparison of measured and calculated focal lengths for hemi-elliptical thermoplastic microlenses as a function of deposited droplet spacing.

## 8.0 CONCLUSIONS

During the performance period of this SBIR contact we have developed a highly viable new technology for ink-jet/micro-jet printing of refractive microlenses, which, by virtue of its low cost and flexibility, could potentially provide significant advantages in many optical-interconnect manufacturing applications. We have demonstrated non-contact printing of plano/convex microlenses with both hemispherical and anamorphic configurations, with substrate plane dimensions from 80  $\mu\text{m}$  to several mm, with speeds variable from  $f/0.7$  to  $f/5$ , with good optical performance characteristics (low absorption and spherical aberrations), with dimensional and focal length reproducibility of better than 1% and 2%, respectively, and with the mechanical and thermal stabilities needed for commercial, high-power applications.

We have pointed out in particular how printed hemi-elliptical microlenses could be ideally suited for both reducing the cost of manufacture and optimizing the efficiency of geometric multiplexing of edge-emitting diode laser arrays into optical fibers, by adjusting both the lenslet configuration (e.g., ratio of "slow"-to-"fast" focal lengths) and their placement on the substrate to remove astigmatism and match the individual characteristics (e.g., emitter locations) of each laser array. Initial experiments with a visible red edge-emitting diode laser source confirmed the validity of this approach and provided quantitative data on lenslet design for this application. It was similarly argued that quasi-hyperbolic microlenses could be printed directly onto VCSEL's (Vertical Cavity Surface Emitting Lasers) for beam collimation or focusing into arrays of optical fibers or detectors.

We have also demonstrated how hemispherical microlenses may be printed onto the tips of optical fibers or detectors for increasing numerical apertures for light collection. Experiments also validated the use of printed arrays of hemispherical microlenses for de-multiplexing focusing of a collimated light source, with good imaging characteristics, or for relatively efficient retro-reflection of collimated laser beams. Models were also developed for printed hemispherical and hemi-elliptical microlenses as caps cut from spheres and ellipsoids, respectively, which facilitate

the optimization of printing parameters to meet particular design specifications.

In short, we have developed an exciting new technology for microlens fabrication which offers the potential for significant benefits in cost reduction and flexibility in numerous optoelectronic manufacturing applications. We may also conclude from this work that microlenses may be printed with this technology which have the breadth of dimensional and quality of optical performance characteristics, the fabrication reproducibility, and the robustness required for commercialization.

Directions for continuation of this work in the future under other U.S. Government and/or commercial sponsorship are quite clear. In general we would work toward increasing precision and reproducibility of microlens printing in order to broaden the spectrum of applications toward which the technology could be applied. In conjunction with this we would focus on obtaining *more quantitative* data on printed microlens performance in many of the proposed beam shaping applications. For example, we would design, print and utilize an iterative development process with edge-emitting diode laser and VCSEL sources to optimize printed microlens capabilities for beam collimation and focusing, then compare the results with those obtained with more conventionally fabricated microlenses. We would also print and test micro-optical devices which cannot be fabricated readily by other methods, such as full "cat's eye" retro-reflectors having arrays of differently sized microlenses printed on opposite sides of an optical substrates.

## 9.0 REFERENCES

1. B.L. Booth, "Recent developments in polymer waveguide technology and applications for data link and optical interconnect systems," *SPIE Proceedings*, Vol.2691, pp.2-8, 1996.
2. W.B. Veldkamp, "Overview of micro-optics: past present and future," *SPIE Proceedings*, Vol.1544, pp.287-299, 1991.
3. B.L. Booth, in Polymers for Electronic and Photonic Applications, C.P. Wong, editor, Academic Press Publishers, Boston, pp. 287-299, 1991.
4. A. Garito., R.F. Shi and M. Wu, "Nonlinear optics of organic and polymer materials," *Physics Today*, May, 1994.
5. T.R. Jay and M.B. Stern, "Preshaping photoresist for refractive microlens fabrication," *Optical Engineering*, Vol.33, No.11, pp.3552-3555, 1994.
6. C.N. Tyssier, "Molded plastic optics enter the mainstream," *Photonics Spectra*, pp.105-110, March, 1996.
7. F. Savart, "Memoire sur la Constitution des Veines Liquides Lancees par des Orifices Circulaires en Mince Paroi," *Annales de Chimie et de Physique*, 53, 337, 1833.
8. Lord Rayleigh, "On the Instability of Jets," *Proc. London Math Soc.*, 10, No. 4 (1878).
9. Lord Rayleigh, *Proc. Roy. Soc.*, Vol. 29, p. 71, 1879.
10. Lord Rayleigh, "On the Instability of a Cylinder of Viscous Liquid Under Capillary Force," *Phil. Mag.*, Vol. 34, no. 145, 1892.
11. C. Weber, "Zum Zerfall eines Flussigkeitsstrables," *Z. Angew. Math. Mech.*, Vol. 11, no. 136, 1931.
12. K.C. Chaudhary, I.G. Redekopp, and T. Maxworthy, "The Non-Linear Capillary Instability of a Liquid Jet," *Journ. Fluid Mech.*, Vol. 96, part II, pp. 257-312, 1979.
13. W.T. Pimbley, "Drop Formation from a Liquid Jet: A Linear One-Dimensional Analysis Considered as a Boundary Value Problem," *IBM Journ. Res. Dev.*, Vol. 29, pp. 148-156, 1984.
14. Hansell, U.S. Patent 2,512,743, 1950.
15. D.B. Bogy and F.E. Talke, "Experimental and Theoretical Study of Wave Propagation Phenomena in Drop-On-Demand Ink Jet Devices," *IBM Journ. Res. Develop.*, Vol. 29, pp. 314-321, 1984.
16. J.F. Dijksman, "Hydrodynamics of Small Tubular Pumps," *Journ. Fluid Mech.*, Vol. 139, pp. 173-191, 1984.

17. D.B. Wallace, "A Method of Characteristics Model of a Drop-On-Demand Ink-Jet Device Using an Integral Method Drop Formation Model," *ASME publication 89-WA/FE-4*, December 1989.
18. W.R. Cox, D.J. Hayes, T. Chen, D.W. Ussery, D.L. MacFarlane and E. Wilson, "Fabrication of micro-optics by microjet printing," *SPIE Proceedings*, Vol.2383, pp.110-115, 1995.
19. W.R. Cox, T. Chen, D.W. Ussery, D.J. Hayes, R.F. Hoenigman, D.L. MacFarlane and E. Rabinovich, "Microjet printing of anamorphic microlens arrays," *SPIE Proceedings*, Vol.2687, pp.89-98, 1996
20. W.R. Cox, D.J. Hayes, T. Chen, H-J Trost, M.E. Grove, R.F. Hoenigman and D.L. MacFarlane, "Low cost optical interconnects by microjet printing," *IMAPS J. Microcircuits & Electronic Packaging*, Vol. 20, No. 2, pp. 89-95, 1997.
21. C.A. Edwards, H.M. Presby and C. Dragone, "Ideal microlenses for laser to fiber coupling," *Journal of Lightwave Technology*, Vol.11, No.2, pp.252-257, February, 1993.
22. W.R. Cox, T. Chen, D. Ussery, D.J. Hayes, J.A. Tatum and D.L. MacFarlane, "Microjetted lenslet tipped fibers," *Optics Communication*, Vol.123, pp.492-496, 1996.
23. W. Zurcher, R. Loser and S. A. Kyle, "Improved reflector for interferometric tracking in three dimensions," *Optical Engineering*, Vol. 34, No. 9, pg. 2740-2743, 1995.
24. E. Hecht and A. Zajac, *Optics*, Addison-Wesley Publishing Company, Reading, MA, pg. 421, 1979.
25. C.S. Williams and O.A. Becklund, *Introduction to the Optical Transfer Function*, John Wiley & Sons, New York, 1989.
26. B.T. Teipen, "Microlens Characterization Using the Modulation Transfer Function," M.S. Thesis, Erik Jonsson School of Engineering and Computer Science, The University of Texas at Dallas, (unpublished) 1997.
27. N. Lindlein, S. Haselbeck and J. Schwider, "Simplified theory for ellipsoidal melted microlenses," *EOS Topical Meeting on Microlens Arrays*, U.K., pp. 7-10, May, 1995.
28. G. B. Thomas and R. L. Finney, *Calculus and Analytic Geometry*, Addison Wesley, Reading, MA pg. 552, 1980.
29. D. L. MacFarlane, "Laser beam alignment devices for ultra short pulses," *Rev. Sci. Instrum.* Vol. 62, pp.1899-1903, 1991.

## DISTRIBUTION LIST

**AUL/LSE**

**Bldg 1405 - 600 Chennault Circle**

**Maxwell AFB, AL 36112-6424** 1 cy

**DTIC/OCP**

**8725 John J. Kingman Rd, Suite 0944**

**Ft Belvoir, VA 22060-6218** 2 cys

**AFSAA/SAI**

**1580 Air Force Pentagon**

**Washington, DC 20330-1580** 1 cy

**AFRL/PSOTL**

**Kirtland AFB, NM 87117-5776** 2 cys

**AFRL/PSOTH**

**Kirtland AFB, NM 87117-5776** 1 cy

**MicroFab Technologies, Inc.**

**1104 Summit Ave., Suite 110**

**Plano, TX 75074** 1 cy

**Official Record Copy**

**AFRL/DELS/Charles E. Moeller** 5 cys